Fluctuating hydrodynamics in periodic domains and heterogeneous adjacent multidomains: Thermal equilibrium

Xin Bian, Zhen Li, Mingge Deng, and George Em Karniadakis

Fluctuating hydrodynamics in periodic domains and heterogeneous adjacent multi-domains. Thermal equilibrium

Xin Bian,[*] Zhen Li, Mingge Deng, and George Em Karniadakis[†]

Division of Applied Mathematics, Brown University, Providence, RI 02912, USA

We first study fluctuating hydrodynamics (FH) at equilibrium in periodic domains by smoothed dissipative particle dynamics (SDPD) method. We examine the performance of SDPD by comparing with the theory of FH. We find that the spatial correlation of particle velocity is always the Dirac delta function, irrespective of numerical resolution, in agreement with the theory. However, the spatial correlation of particle density has a finite range of r_c, which is due to the kernel smoothing procedure for the density. Nevertheless, this finite range of correlation can be reduced to an arbitrarily small value by increasing the resolution, that is, reducing r_c, similarly to how the smoothing kernel converges to the Dirac delta function. Moreover, we consider temporal correlation functions (CFs) of random field variables in Fourier space. For sufficient resolution, the CFs of SDPD simulations agree very well with analytical solutions of the linearized FH equations. This confirms that both the shear and sound modes are modeled accurately, and that fluctuations are generated, transported and dissipated in both thermodynamically and hydrodynamically consistent ways in SDPD. We also show that the CFs of the classical dissipative particle dynamics (DPD) method with proper parameters can recover very well the linearized solutions. As a reverse implication, the measurement of CFs provides an effective means of extracting viscosities and sound speed of a DPD system with a new set of input parameters.

Subsequently, we study the FH in truncated domains in the context of multiscale coupling via the domain decomposition method, where a SDPD simulation in one sub-domain is coupled with a NS solver in an adjacent sub-domain with an overlapping region. At equilibrium, the mean values of the NS solution are known *a priori* and do not need to be extracted from actual simulations. To this end, we model a buffer region as an equilibrium boundary condition (EBC) at the truncated side of the SDPD simulation. In the EBC buffer, the velocity of particles is drawn from a known Gaussian distribution, that is, the Maxwell-Boltzmann distribution. Due to the finite range of spatial correlation, the density of particles in the EBC buffer must be drawn from a *conditional* Gaussian distribution, which takes into account the available density distribution of neighboring interior particles. We introduce a Kriging method to provide such a conditional distribution and hence preserve the spatial correlation of density. Spatial and temporal correlations of SDPD simulations in the truncated domain are compared to that in a single complete domain. We find that a gap region between the buffer and interior is important to reduce the extra dissipation generated by the artificial buffer at equilibrium, rendering more investigations necessary for thermal fluctuations in the multiscale coupling of nonequilibrium flows.

I. INTRODUCTION

Hydrodynamic fluctuations arise in a mesoscopic volume of fluid and play a crucial role in polymer physics, colloidal dynamics and biological science. From a continuum perspective, such mesoscopic phenomena may be well described by the Landau-Lifshitz Navier-Stokes (LLNS) equations [1]. Accordingly, numerical methods can be immediately obtained by a direct discretization of the LLNS equations; for example, thermal fluctuations have been incorporated in the finite volume method (FVM) [2] and the smoothed particle hydrodynamics method (SPH) [3] in such a way. Alternatively, the fluctuating hydrodynamics (FH) may be interpreted from a coarse-grained perspective and a few simulation tools do exist, such as, the lattice-Boltzmann method [4], the dissipative particle dynamics (DPD) method [5–7], and the

stochastic rotational dynamics/multiple particle collision dynamics (SRD/MPCD) method [8].

Smoothed dissipative particle dynamics (SDPD) method is formulated by bridging the two distinct perspectives [9]. In particular, its original derivation starts from a SPH discretization of the Navier-Stokes (NS) equations, and thereafter, introduces thermal fluctuations *directly on the discrete particle level* according to the GENERIC (general equation for the nonequilibrium reversible-irreversible coupling) structure [10]. The conservative, dissipative, and stochastic forces in SDPD are expressed in a pairwise formulation, which resembles the classical DPD method, therefore it is named as smoothed DPD. Due to the GENERIC formalism and the way thermal fluctuations are introduced, there are a few prominent features of SDPD method: fluctuation-dissipation theorem (FDT) and the first/second law of thermodynamics are *strictly* satisfied on the discrete particle level [9], and the scaling of fluctuations follows the length scale of the particles [11]. Similarly, this combined perspective is also adopted to attain the thermal fluctuations for a FVM discretization of the NS equations [12, 13].

---
[*] xin_bian@brown.edu
[†] george_karniadakis@brown.edu

SDPD has been successfully applied in modeling complex fluids at mesoscale, such as, polymer solution [14], colloid suspension [15, 16] blood flow with cells [17], and hydrophobicity [18], although it neither directly discretizes the LLNS equations, nor it is obtained by a systematic coarse-graining procedure. The original developers interpreted SDPD method as a discrete Lagrangian version of FH based on the following assumption [9]: each SDPD particle represents a thermodynamic subsystem at local equilibrium. Therefore, according to the theory of FH [1, 2, 19, 20], one should not expect spatial correlations of density and velocity between SDPD particles within a finite range. Hence, the first goal of this work is to *explicitly* identify the one-to-one correspondence between SDPD and FH at equilibrium. In particular, we pay attention not only to the spatial correlations, but also to the temporal correlation functions (CFs) of the random state variables, which encompass both the shear and sound modes. Since the analytical solutions of the linearized FH are available in periodic domains, it can help us quantify the discrepancy, if any, between SDPD simulations and FH. Moreover, we also verify if the classical DPD method can faithfully recover the analytical solutions of CFs in the linear regime.

Subsequently, we study the FH simulations in "truncated" domains. This is a fundamental scenario in the context of multiscale coupling via the domain decomposition (DD) method. In the recent past, the multiscale coupling has attracted a lot of research interest [21–34], to combine the computational advantage of a coarse model and the accurate description of a fine model. Very often, on one side of the coupling is a stochastic system, such as, the DPD method [30], or the molecular dynamics (MD) [21]. On the other side of the coupling there is either a deterministic system (such as a FVM [29] and a spectral element method [30]), or a stochastic system (such as a coarse-grained MD and a FH solver [27, 28]). The main achievements of the past have been the steady/transient mean velocity profiles for nonequilibrium flows and external perturbations, whereas very little effort was paid to thermal fluctuations. With the exception of some work [26, 28], which allow uncertainties to propagate across different scales, thermal fluctuations are actually often considered as unwanted noises to average out. However, simply filtering out the thermal fluctuations would invalidate the original motivation of introducing them in the first place. More specifically, there is little effort so far to evaluate rigorously how well the fluctuations are generated, transported and dissipated in the presence of a hybrid interface between simulations of different scales. Especially on the side of the fine scale, extra degrees of freedom are underdetermined and usually assigned artificial values from certain (e.g., Gaussian) distributions, which inevitably introduces artificial dissipations into the coupled system. Hence, the second goal of this work is to quantify "how much" of the fluctuations is preserved in the context of multiscale coupling by measuring the artificial dissipations due to the hybrid interface. Therefore,
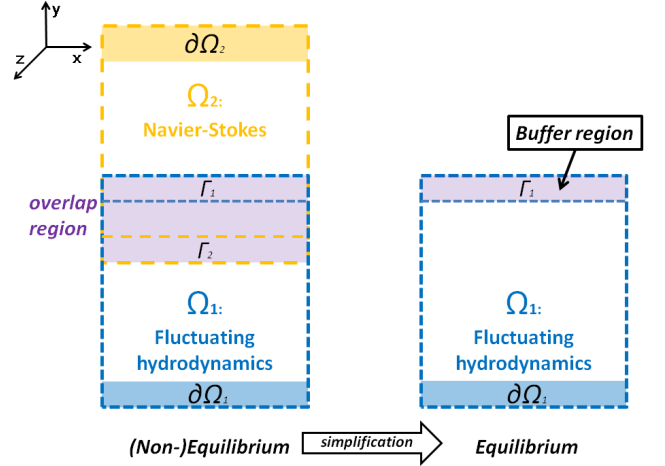

Figure 1: (Color online) Simplification for multiscale coupling of heterogeneous adjacent multi-domains at equilibrium: on the left is a sketch of multiscale coupling between a Navier-Stokes (NS) solver with a fluctuating hydrodynamics (FH) solver via the domain decomposition (DD) method. In particular, a solver of FH in $\Omega_1 \cup \partial\Omega_1 \cup \Gamma_1$ is coupled with a solver of the NS equations in $\Omega_2 \cup \partial\Omega_2 \cup \Gamma_2$. $\partial\Omega_1$ and $\partial\Omega_2$ are external boundaries. Γ_1 and Γ_2 are artificial boundaries embedded in each other's interior region, respectively. On the right, the DD method can be simplified at equilibrium by removing the NS solver, but retaining the stochastic artificial boundary Γ_1 for the FH solver. The density and velocity fields in Γ_1 are drawn from (conditional) Gaussian distributions with known means and variances.

we focus on the thermal equilibrium state and disregard any NS solver on the other side of the coupling. This simplification is well sketched in Fig. 1, where all the mean values are known *a priori* on the side of NS and do not need to be extracted from actual simulations. To this end, we do not perform any NS simulation, but instead model a buffer region Γ_1 as the equilibrium boundary condition (EBC) with known means and variances for velocity and density at the truncated side of a FH simulation along y direction. The other side along y direction is wall-bounded and periodic boundary condition is applied in the other direction. We adopt SDPD as an effective FH solver in the truncated domain. To preserve the spatial correlation of density for SDPD particles near Γ_1, we introduce a Kriging method to provide conditional Gaussian distributions. We will evaluate results of statistics, spatial correlations, and temporal CFs for the SDPD simulations in the truncated domain by comparing them at the same region with SDPD simulations in a single/complete wall-bounded domain (see Fig. 10).

The rest of this paper is organized as follows. In Section II, we briefly review the standard formulation of the SDPD method and focus on the isothermal case. In Sec-

tion III, we compute some statistics, spatial correlations, and temporal CFs of SDPD state variables in periodic domains. Moreover, we compare results of SDPD with the theory of FH in the linear regime, where the analytical expressions for CFs are available. In Section IV, we describe a Kriging method to preserve the spatial correlation of density in the SDPD simulations in truncated domains. Furthermore, we compare statistics, spatial and temporal CFs in the truncated simulations with reference solutions. Finally, we summarize this work with discussions in the context of multiscale coupling in Section V.

II. SMOOTHED DISSIPATIVE PARTICLE DYNAMICS

We start with a brief description of the smoothed particle hydrodynamics (SPH) method [35] and subsequently we introduce its extension to obtain the standard SDPD method [9].

For convenience, we define some simple notations as reference

$$
\begin{aligned}
\mathbf{r}_{ij} &= \mathbf{r}_i - \mathbf{r}_j, \\
\mathbf{v}_{ij} &= \mathbf{v}_i - \mathbf{v}_j, \\
\mathbf{e}_{ij} &= \mathbf{r}_{ij}/r_{ij}, \quad r_{ij} = |\mathbf{r}_{ij}|,
\end{aligned}
\tag{1}
$$

where $\mathbf{r}_i$, $\mathbf{v}_i$ are position and velocity of particle i; $\mathbf{r}_{ij}$, $\mathbf{v}_{ij}$ are relative position and velocity of particles i and j; r_{ij} is the distance of the two and $\mathbf{e}_{ij}$ is the unit vector pointing j to i. The equation of motion for SPH particles and the corresponding discrete continuity and momentum equations are:

$$
\dot{\mathbf{r}}_i = \mathbf{v}_i,
\tag{2}
$$

$$
d_i = \frac{\rho_i}{m_i} = \sum_j W(r_{ij}) = \sum_j W_{ij},
\tag{3}
$$

$$
m_i \dot{\mathbf{v}}_i = \sum_{j \neq i} \left(\mathbf{F}_{ij}^C + \mathbf{F}_{ij}^D \right),
\tag{4}
$$

where d is particle number density defined as the ratio of density ρ and particle mass m (constant), and it is calculated based on neighboring particle positions. $W(r)$ is a bell-shaped weighting function called "SPH kernel", and it has at least two properties

$$
\lim_{h \to 0} W(\mathbf{r} - \mathbf{r}', h) = \delta(\mathbf{r} - \mathbf{r}'), \quad \int W(\mathbf{r} - \mathbf{r}', h) d\mathbf{r}' = 1,
\tag{5}
$$

where h is defined as smoothing length. Any kernel adopted should converge to the Dirac delta function $\delta(\mathbf{r})$ as $h \to 0$ and its integral must be normalized. In this work the quintic kernel from the B-spline family is adopted (see Appendix A) and the cut off radius $r_c = 3h$ is based on user's choice to limit numerical errors. Note that Eqs. (2) and (3) account for the continuity equation, which does not need to be explicitly discretized [9, 35].

$\mathbf{F}_{ij}^C$ and $\mathbf{F}_{ij}^D$ are pairwise forces between particles, which are conservative and dissipative, respectively, and

they correspond to a discretization of forces due to pressure and viscous stress in the Navier-Stokes (NS) equations. Following a thermodynamic framework, an expression for the conservative force is obtained as follows [9],

$$
\mathbf{F}_{ij}^C = - \left(\frac{P_i}{d_i^2} + \frac{P_j}{d_j^2} \right) \frac{\partial W}{\partial r_{ij}} \mathbf{e}_{ij},
\tag{6}
$$

which was also previously derived more rigorously and has been widely utilized [35]. Eq. (6) proves to be also variationally consistent with the density summation Eq. (3) [36]. $\mathbf{F}_{ij}^C = -\mathbf{F}_{ji}^C$ (Newton's 3rd law) and they are active along $\mathbf{e}_{ij}$, therefore both linear and angular momenta are strictly conserved. The pairwise viscous forces between particle i and j can be discretized as [9],

$$
\mathbf{F}_{ij}^D = \frac{\eta}{d_i d_j r_{ij}} \frac{\partial W}{\partial r_{ij}} \left(\frac{2D - 1}{D} \mathbf{v}_{ij} + \frac{D + 2}{D} \mathbf{e}_{ij} \cdot \mathbf{v}_{ij} \mathbf{e}_{ij} \right),
\tag{7}
$$

where the dimension D ($= 2$ or 3) of the problem is explicitly introduced into the discretization. $\mathbf{F}_{ij}^D$ also satisfies Newton's 3rd law so that it conserves linear momentum.

An equation of state (EOS) relating pressure to density is needed to provide a closure for the weakly compressible description. We consider a linear EOS sufficient for the following analysis,

$$
p = c_T^2 \rho,
\tag{8}
$$

where the artificial sound speed c_T is chosen based on a scale analysis [35, 37] such that the pressure field reacts strongly to small deviations in density and weak compressibility is fulfilled. We also consider another stiff EOS [35, 38],

$$
p = \frac{c_T^2 \rho_e}{7} \left[\left(\frac{\rho}{\rho_e} \right)^7 - 1 \right] + \chi,
\tag{9}
$$

where ρ_e is the equilibrium density and χ is a constant to ensure positive pressure on each particle. However, the following results are not sensitive to the EOS selected and we will only report results by Eq. (8).

Following the GENERIC framework [10], a pairwise random force is introduced directly on the discrete particle as [9, 11]

$$
\begin{aligned}
\mathbf{F}_{ij}^R &= \left(\frac{-20 \eta k_B T}{3 d_i d_j r_{ij} \Delta t} \frac{\partial W}{\partial r_{ij}} \right)^{1/2} d\overline{\mathbf{W}}_{ij} \cdot \mathbf{e}_{ij}, \\
d\overline{\mathbf{W}}_{ij} &= \frac{1}{2} \left(d\mathbf{W}_{ij} + d\mathbf{W}_{ij}^T \right),
\end{aligned}
\tag{10}
$$

where $d\mathbf{W}$ is a matrix of independent increments of Wiener process. Therefore, the momentum equation of Eq. (4) is extended for SDPD particles as

$$
m_i \dot{\mathbf{v}}_i = \sum_{j \neq i} \left(\mathbf{F}_{ij}^C + \mathbf{F}_{ij}^D + \mathbf{F}_{ij}^R \right).
\tag{11}
$$

We adopt the velocity Verlet integrator for the time integration of SDPD particles (see Appendix B). To maintain numerical stability of the explicit scheme, the time-step size Δt is restricted by two conditions [37]: $\Delta t \leq 0.25h/c_T$ and $\Delta t \leq 0.125h^2/\nu$ (kinematic viscosity $\nu = \eta/\rho$). For high resolution in viscous flows, the squared dependence on h usually dominates.

III. FLUCTUATING HYDRODYNAMICS IN PERIODIC DOMAINS

The SDPD method was first proposed as a discrete Lagrangian version of fluctuating hydrodynamics (FH) [9]. Here we *explicitly* examine its statistics, spatial correlations, and temporal correlations by comparing with available theoretical results of FH. In the following simulations, we take units such that density $\rho = 1$, box length $L_x(= L_y = L_z) = 1$, thermal energy $k_B T = 1$ (k_B is Boltzmann's constant and T is temperature), and dynamic viscosity $\eta = 49.71$. The isothermal sound speed c_T is taken as some multiple times of the thermal speed v_T of SDPD particles to keep the density variation within a small percentage. We note that c_T is artificial and usually smaller than the real sound speed, yet it is the actual sound speed in the simulations.

A typical SDPD simulation starts with particles on cubic/square lattice with spacing $\Delta x = 0.05$ and $r_c = 3\Delta x = 0.15$ in a periodic box. Therefore, in $2D$ each particle mass $m = \rho \Delta x^2 = 2.5 \times 10^{-3}$. A priori estimation of the fluctuating magnitude of velocity is $v_T = \sqrt{2k_B T/m} \approx 28$, where v_T is taken as the standard deviation of velocity. Similarly in $3D$, $m = \rho \Delta x^3 = 1.25 \times 10^{-4}$ and $v_T = \sqrt{3k_B T/m} \approx 155$.

A. Some statistics

Firstly, we examine the probability distribution functions (PDFs) for velocity and density of SDPD particles. SDPD simulations run in an extended box $[2L_x, 2L_y] = [2, 2]$ with $N = 1600$ particles to have more statistics. Here $c_T = 600 \gtrsim 20v_T$ is taken so that maximum density variation is $\sim 5\%$. $\Delta t = 1.4 \times 10^{-5}$. Computing the PDFs is based on 10^4 steps only after the first 10^3 steps of equilibration. The computed PDFs are shown in Fig. 2. Theoretically, the PDF for the velocity should coincide with the celebrated Maxwell-Boltzmann distribution in each dimension

$$P(v) = \sqrt{\frac{m}{2\pi k_B T}} exp\left(\frac{-mv^2}{2k_B T}\right), \qquad (12)$$

which is true for SDPD particles as shown in Fig. 2(a). A Gaussian fit of the data (the variance) indicates that the relative error of SDPD temperature compared to the input one falls well below 1%. This also corroborates the results of previous works [11, 39].
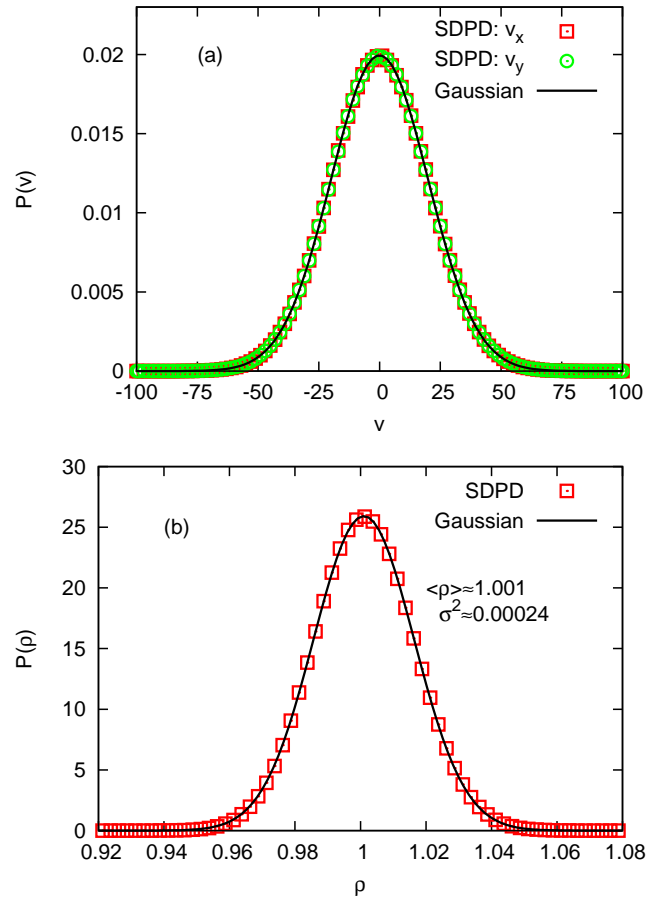

Figure 2: (Color online) Probability distribution functions (PDFs) for velocity and density of SDPD particles. (a) velocity: solid line is the Maxwell-Boltzmann distribution. (b) density: solid line is the best Gaussian fit with mean $< \rho > \approx 1.001$ and variance $\sigma^2 \approx 0.00024$.

The PDF for the density of SDPD particles can also be fitted very well with a Gaussian distribution, as shown in Fig. 2(b). However, the measured mean differs slightly ($\approx 0.1\%$) from the expectation of equilibrium density ρ_e, which should be unity. This is due to the SPH kernel interpolation for density, which has a small bias on non-random data points (see, for example, Ref [40] for an extensive discussion).

To explicitly validate that the PDFs of velocity and density for SDPD particles are indeed Gaussian with symmetric distributions, we also calculate the quantile-quantile (Q-Q) plot for both quantities, as shown in Appendix C. We observe that both Q-Q plots have clearly linear slopes, which indicate a negligible skewness on the PDFs of Fig. 2.

In the Eulerian framework, the variance of density can be predicted by the grand canonical ensemble as [1, 13,
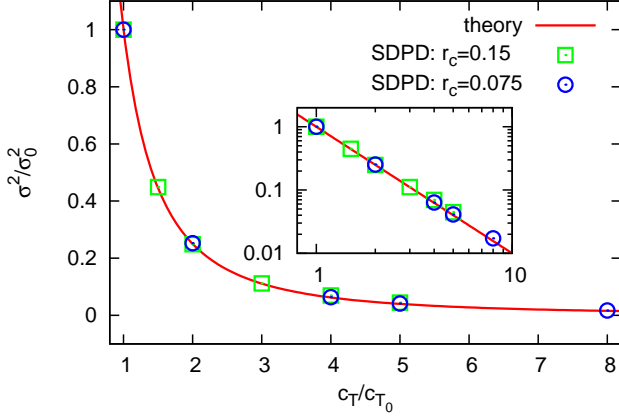
Figure 3: (Color online) Density variance versus sound speed. The inset shows the same data in logarithm-logarithm scale. The theory is $1/x^2$ derived from Eq. (13).
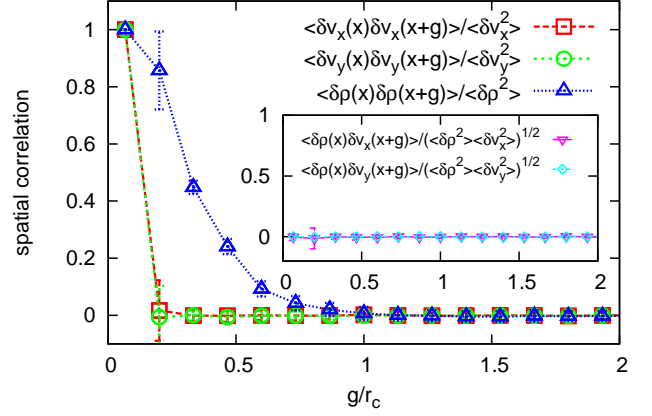

Figure 4: (Color online) Spatial correlations of velocity and density for SDPD particles: $r_c = 0.15$ and $c_T = 600$. The inset shows the cross correlation between density and velocity. Error bars are standard deviations of $N_s = 50$ independent runs.

19]

$$\sigma^2(\rho) = \frac{\rho_e k_B T}{c_T^2 V_c}, \qquad (13)$$

where V_c is the volume of an Eulerian cell fixed in space. In the Lagrangian framework, we expect that the variance of SDPD density is also proportional to d_e/c_T^2, where $d_e = 1/V_c$ is the equilibrium number density. We perform two sets of simulations at two different resolutions, that is, $r_c = 3\Delta x = 0.15$ and $r_c = 3\Delta x = 0.075$, which correspond to number density $d_e = 400$ and 1600, respectively. The sound speed c_T varies from 300 to 2400. We present the density variance versus the sound speed in Fig. 3, where the sound speed is rescaled by $c_{T_0} = 300$ and the variance is rescaled by the variance at $c_{T_0} = 300$. From the computed results, we can conclude that the density variance of SDPD indeed behaves as

$$\sigma^2(\rho) \sim \frac{d_e k_B T}{c_T^2}. \qquad (14)$$

B. Spatial correlations

In this section, we further assess the spatial covariance, correlation and semivariance between the random state variables of SDPD particles. The covariance is defined as

$$C_v(\mathbf{g}) = \frac{1}{N(\mathbf{g})} \sum_{i=1}^{N(\mathbf{g})} [u(\mathbf{x}_i) - \overline{u}] \cdot [w(\mathbf{x}_i + \mathbf{g}) - \overline{w}],$$

$$= \frac{1}{N(\mathbf{g})} \sum_{i=1}^{N(\mathbf{g})} \delta u(\mathbf{x}_i) \cdot \delta w(\mathbf{x}_i + \mathbf{g}), \qquad (15)$$

where the variables u and w may be different or the same, and is one of the state variables (ρ, v_x, and v_y). $\overline{u}$ and

$\overline{w}$ are their expectations or means, $\mathbf{g}$ is the displacement vector, and $N(\mathbf{g})$ is the number of samples. The correlation coefficient is the covariance normalized by the variances as

$$C_r(\mathbf{g}) = C_v(\mathbf{g})/\sqrt{\sigma_u^2 \sigma_w^2}. \qquad (16)$$

The semivariance is also a related concept and will be useful later in Section IV A. It is defined as

$$S(\mathbf{g}) = \frac{1}{2N(\mathbf{g})} \sum_{i=1}^{N(\mathbf{g})} [u(\mathbf{x}_i) - u(\mathbf{x}_i + \mathbf{g})]^2. \qquad (17)$$

The density and velocity of SDPD particles with the same simulation parameter as in Section III A are indexed in Eulerian bins before applying Eqs. (15), (16) and (17). Spatial correlations are shown in Fig. 4, where the error bar indicates the standard deviations ($\sqrt{\sigma^2}$) of $N_s = 50$ independent runs. The standard deviations are smaller than or similar in size of the symbols except at the second bin. The relatively large deviation in the second bin can be understood by taking into account the radial distribution function (RDF) of SDPD particles, as shown in Fig. 5. The "repelling" zone ($g/r_c \lesssim 0.2$) of SDPD particles in Fig. 5 is due to the strong conservative force $\mathbf{F}_{ij}^C$ at short distance. As a consequence, the statistics in the second bin are noisy in Fig. 4. We further note that the repelling zone is not a negative property overall, together with the semi-glassy structures indicated by the first and second peaks in Fig. 5, they minimize the discretization error of Lagrangian particle methods [35, 41].

The standard error ($\sqrt{\sigma^2/N_s}$) in each bin is always smaller than the symbol size, therefore it is safe to conclude that the spatial correlation for velocity is the Dirac delta function, whereas for density has a finite range of r_c. We explicitly confirm this conclusion further by increasing and decreasing the resolution and perform another
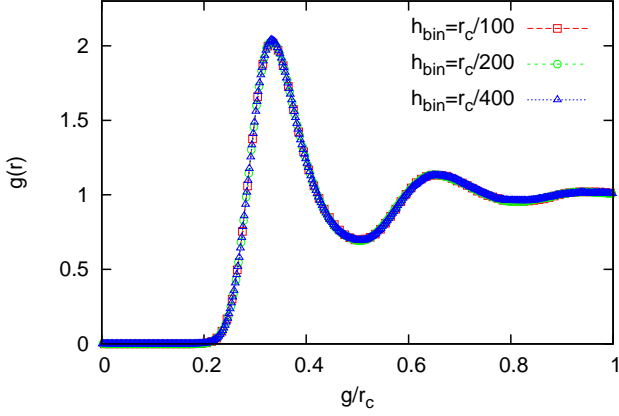
Figure 5: (Color online) Radial distribution function (RDF) of SDPD particles with three bin-sizes: $r_c = 0.15$ and $c_T = 600$. The result is not sensitive to different bin-sizes used for averaging.

Figure 6: (Color online) The dependence of spatial correlation of SDPD particles on r_c. (a) v_x. (b) ρ. $r_c/\Delta x = 3$ is fixed and $c_T = 600$.

$50 + 50$ independent runs. The dependence of spatial correlations on r_c is shown in Fig. 6, where for velocity it is always the Dirac delta function and for density it always has a finite range of r_c.

We further calculate the density-velocity cross spatial correlation of SDPD particles, which is a spatially constant *zero*, as shown in the inset of Fig. 4, where the error bars are in the order of 1% except in the second bin where the error bar is 8.6%.

From the theory of FH [1, 2, 13, 19, 20], the spatial correlations at equilibrium are known as

$$< \delta\rho(\mathbf{x}_i) \cdot \delta\rho(\mathbf{x}_j) > = \sigma_\rho^2 \delta(|\mathbf{x}_i - \mathbf{x}_j|), \quad (18)$$

$$< \delta v(\mathbf{x}_i) \cdot \delta v(\mathbf{x}_j) > = \sigma_v^2 \delta(|\mathbf{x}_i - \mathbf{x}_j|), \quad (19)$$

$$< \delta\rho(\mathbf{x}_i) \cdot \delta v(\mathbf{x}_j) > = 0, \quad (20)$$

where σ_ρ^2 and σ_v^2 are the variances of density and velocity. Therefore, we can conclude that the spatial correlation for velocity of SDPD particles agrees very well with the theory, and so does the density-velocity cross correlation. However, the spatial correlation for density of SDPD particles always has a finite range, which deviates from the theory. This is due to the fact that density of SDPD particles is calculated by applying the SPH kernel on neighboring particles as in Eq. (3), therefore any two particles in the neighborhood of r_c have mutual contributions to each other's density and they share partially the same neighboring particles. Nevertheless, the finite range can be reduced arbitrarily small as shown in Fig. 6(b), similarly to how the SPH kernel function approaches the Dirac delta function in Eq. (5).

We will present the semivariance for density of SDPD particles in Section IV A, where it is utilized in the Kriging method to preserve the spatial correlation.
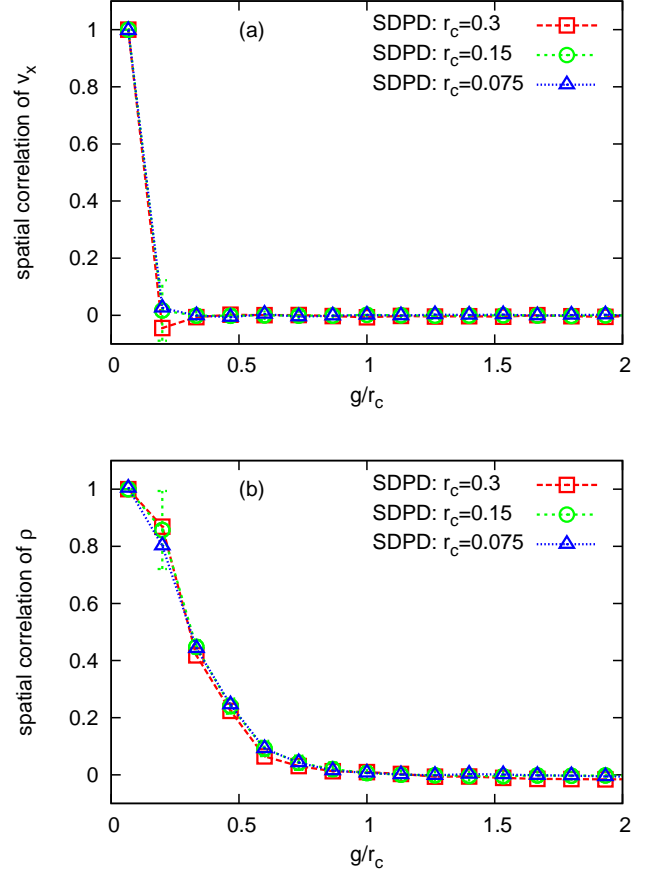
C. Temporal correlations

We proceed to compare the temporal correlation functions (CFs) of SDPD simulations with available analytical solutions at equilibrium. For fluctuations of very small amplitude on density and velocity, the relaxation of the fluid towards equilibrium is described accurately by the *linearized* version of the hydrodynamic equations [19, 20]. The temporal CFs of the fluctuating variables in Fourier space can be solved analytically as [13, 19, 20]

$$\frac{< g_\perp(k,t)g_\perp(k,t+\tau) >}{\sigma^2[g_\perp(k,t)]} = e^{-\nu k^2\tau}, \tag{21a}$$

$$\frac{< g_{||}(k,t)g_{||}(k,t+\tau) >}{\sigma^2\left[g_{||}(k,t)\right]} = e^{-\Gamma_T k^2\tau}cos(c_T k\tau), \tag{21b}$$

$$\frac{< \rho(k,t)\rho(k,t+\tau) >}{\sigma^2\left[\rho(k,t)\right]} = e^{-\Gamma_T k^2\tau}cos(c_T k\tau), \tag{21c}$$

$$\frac{< g_{||}(k,t)i\rho(k,t+\tau) >}{\sigma^2\left[g_{||}(k,t)\right]/c_T} = e^{-\Gamma_T k^2\tau}sin(c_T k\tau), \tag{21d}$$

$$\frac{< \rho(k,t)ig_{||}(k,t+\tau) >}{\sigma^2\left[g_{||}(k,t)\right]/c_T} = -e^{-\Gamma_T k^2\tau}sin(c_T k\tau), \tag{21e}$$

where the wave vector $\mathbf{k} = (k,0,0)$ and $k = 2\pi n_w/L$. Also, n_w is a positive integer number and L is the box length in the direction of wave vector; $\Gamma_T = 2\nu/3$ is the isothermal sound absorption coefficient; $g_\perp$ indicates the transversal component of momentum density perpendicular to $\mathbf{k}$ while $g_{||}$ indicates the longitudinal component of momentum density parallel to $\mathbf{k}$.

For two fluctuating state variables $u(\mathbf{x},t)$ and $w(\mathbf{x},t)$ which may be $\delta v_x(\mathbf{x},t)\rho(\mathbf{x},t)$, $\delta v_y(\mathbf{x},t)\rho(\mathbf{x},t)$, $\delta v_z(\mathbf{x},t)\rho(\mathbf{x},t)$ or $\delta\rho(\mathbf{x},t)$ of SDPD particle at location $\mathbf{x}:(x,y,z)$ and time instant t, we define the CF in Fourier space as

$$< u(k,t)w(k,t+\tau) >= \frac{1}{N_s}\sum_{s=1}^{N_s} \hat{f}_k(u(\mathbf{x},t))\hat{f}_k(w(\mathbf{x},t+\tau)), \tag{22}$$

where N_s is the number of independent simulation runs. The form of the transformed component is defined as

$$\hat{f}_k(u(\mathbf{x},t)) = \frac{1}{N_p}\sum_{j=1}^{N_p} u(\mathbf{x_j},t)e^{-i\mathbf{k}\cdot\mathbf{x}_j(t)}, \tag{23}$$

where j is particle index and N_p is the number of particles in each simulation [42].

Note that we do not project the particle variables onto a grid before calculating its Fourier transform, as the particle's spatial distribution is uniform and isotropic at equilibrium, which allows us to take a direct transform of particle values in a single direction along the wave vector. For non-uniform particle distributions at non-equilibrium, one should consider algorithms for nonequispaced fast Fourier transform (NFFT), for example, Ref. [43].

A typical simulation runs in an extended box $[2L_x, 2L_y] = [2,2]$ with $r_c = 3\Delta x = 0.15$, which has ~ 40 particles spanning over each direction. To guarantee a linear regime, where the analytical solutions in Eq. (21) are valid, we first calibrate the sound speed c_T to have a vanishing small density variation, which is studied also in Fig. 3. We select $c_T = 1200 \approx 40v_T$, to restrict density standard deviation to be $\delta\rho/\rho_e \approx 0.8\%$; also $\Delta t = 1.4 \times 10^{-5}$. We perform $N_s = 50$ independent simulations to obtain average of all initial conditions and

consider three wave numbers, that is, $n_w = 1$, 2, and 4, to examine the thermodynamic and hydrodynamic properties of SDPD at three different length scales, that is, 2 (the box length), 1 and 0.5.

After applying the procedure described in Eqs. (22) and (23), we present the resultant autocorrelation functions (ACFs) in Fig. 7. For the transversal ACF, which is purely due to the shear modes, we rescale time by νk^2 so that results of different wave numbers can be compared directly to each other and with the theory, as shown in Fig. 7(a). SDPD agrees well with the theory at two large length scales 2 and 1 ($n_w = 1$ and 2, respectively), but deviates from the analytical results at small length scale 0.5 ($n_w = 4$), with ~ 10 particles for one wavelength. Since SDPD is a top-down continuum approach, the deviation is purely due to the insufficient numerical resolution at length scale 0.5.

Moreover, we plot the longitudinal and density ACFs in Fig. 7(b) and 7(c), where time is rescaled by $c_T k$ so that results of different wave numbers can be compared directly to each other and with the theory. Similarly to the transversal component, the ACFs for longitudinal component and density of SDPD behaves very well at large length scales, but start to deviate from the analytical solutions also at small wavelength 0.5, which encompasses only ~ 10 particles.

Finally, we calculate the cross correlation functions (CCFs) between the longitudinal momentum density and density, where the analytical expression is anti-symmetric with time between the two quantities. Results of SDPD simulations with time rescaled by $c_T k$ are shown in Fig. 8, where overall good agreements between simulations and analytical expressions are observed. Surprisingly, even at the small length scale 0.5 ($n_w = 4$), the discrepancy between simulations and theory is negligible. This may be due to the Lagrangian nature of the method, which resolves well the correlation between density and longitudinal velocity component.

From results in Figs. 7 and 8, we may conclude that in the *linear regime*, SDPD indeed represents very well the FH, provided the numerical resolution is sufficient. The fluctuation-dissipation balance built in SDPD on the discrete particle level by the GENERIC framework indeed works effectively.

To check the sensitivity of sound speed for the CFs in the simulations, we show results of SDPD with $c_T = 600$ ($\delta\rho/\rho_e \approx 1.5\%$) and $c_T = 300$ ($\delta\rho/\rho_e \approx 3.1\%$) in Fig. 9. We observe a good agreement between simulations with $c_T = 600$ and the theory at all wavelengths, except at wave number $n_w = 4$, where the resolution of SDPD is too low. By further decreasing the sound speed to be $c_T = 300$, the deviations between simulations and the theory become apparent. One might wonder if there is discrepancy between the effective equation of state (EOS) and the one we intend to model (Eq. (8)). However, our calculations of the pressure at various sound speeds do not indicate any inconsistency of the EOS (Appendix D). The disagreement is due to a significant numerical
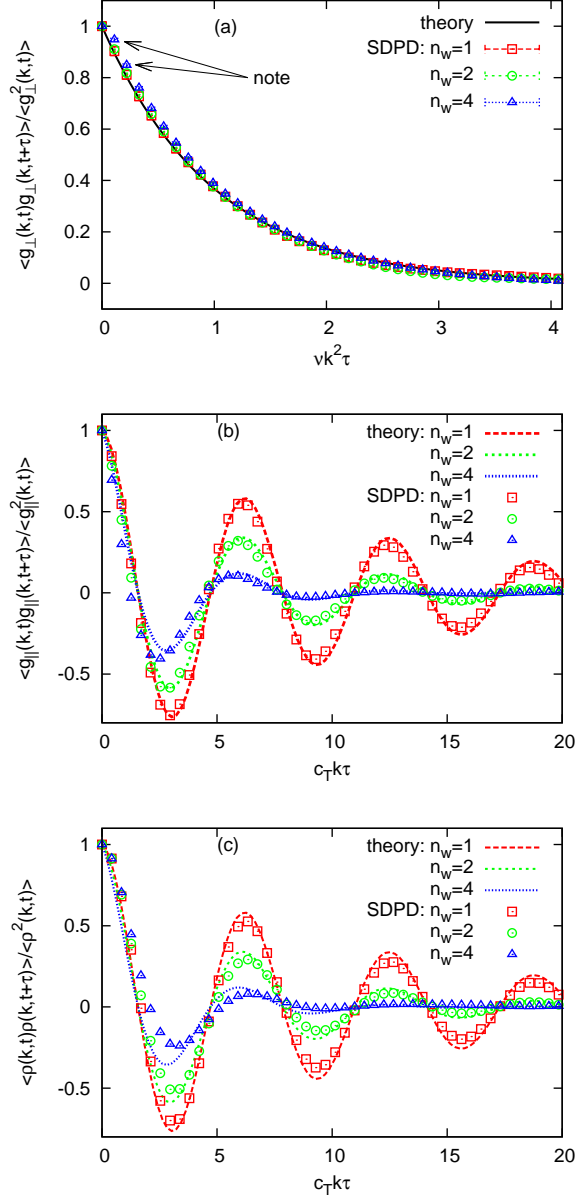
Figure 7: (Color online) Autocorrelation functions in Fourier space for SDPD particles. (a) transversal. (b) longitudinal. (c) density. $r_c = 0.15, c_T = 1200$ and $\delta\rho/\rho_e \approx 0.8\%$. Standard errors are similar to or smaller than the size of the symbols.

error of the weakly compressible description of SDPD method at this particular parameter set with $c_T = 300$ (see Appendix E for an explanation).

In passing, we also compute the ACFs for the classical dissipative particle dynamics (DPD) method in the linear regime and present the results in Appendix F.
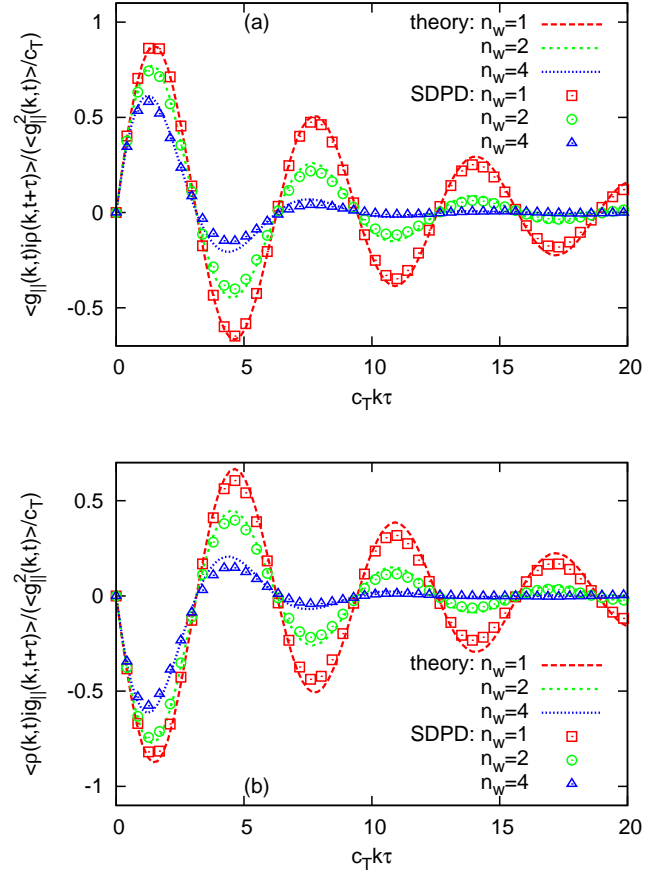

Figure 8: (Color online) Cross correlation functions in Fourier space for SDPD particles. (a) longitudinal-density. (b) density-longitudinal. $r_c = 0.15$, $c_T = 1200$ and $\delta\rho/\rho_e \approx 0.8\%$. Standard errors are similar to or smaller than the size of the symbols.

IV. FLUCTUATING HYDRODYNAMICS IN HETEROGENEOUS ADJACENT MULTI-DOMAINS

In this section, we consider a scenario of SDPD simulations in truncated domains in the context of multiscale coupling via the DD method. We shall consider thermal equilibrium state, to focus on the fluctuating quantities. Therefore, any NS solver can be removed, as sketched in Fig. 1, since all the mean values are known *a priori*. To this end, we model a buffer region as the *equilibrium boundary condition (EBC)* at the truncated side ($L_y \leq y \leq L_y + r_c$) of SDPD simulations. The other side of the simulation ($y \leq 0$) is wall-bounded and periodic boundary is applied in the other direction. We shall take complete and single SDPD simulations in a wall-bounded domain as the "true" solution for reference, as sketched in Fig. 10. where the shadowed fluid regions will be compared to each other.

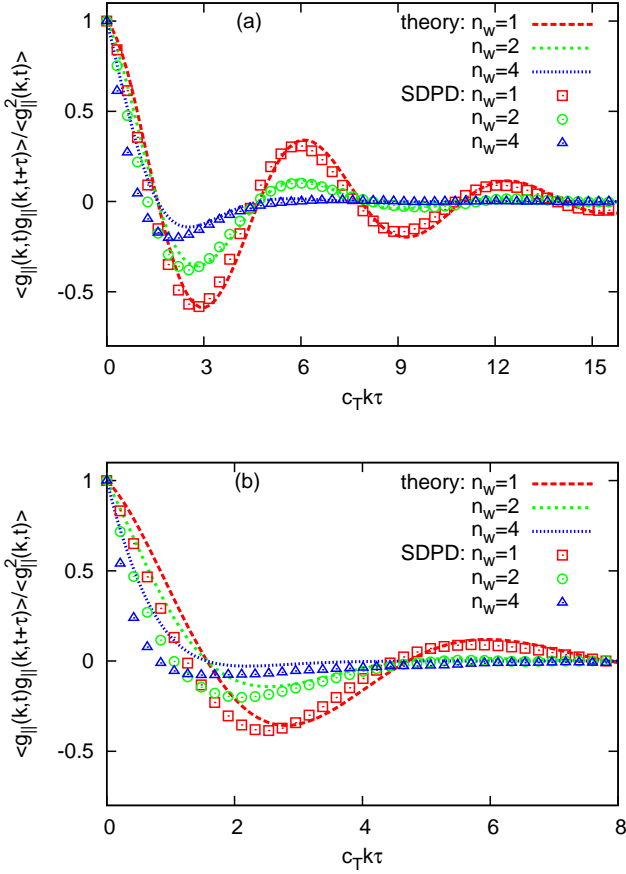Since spatial correlation for velocity of SDPD particles

Figure 9: (Color online) Sensitivity of the sound speed for the autocorrelation function of the longitudinal velocity component in Fourier space for SDPD particles. (a) $c_T = 600$ and $\delta\rho/\rho_e \approx 1.5\%$. (b) $c_T = 300$ and $\delta\rho/\rho_e \approx 3.1\%$. $r_c = 0.15$.
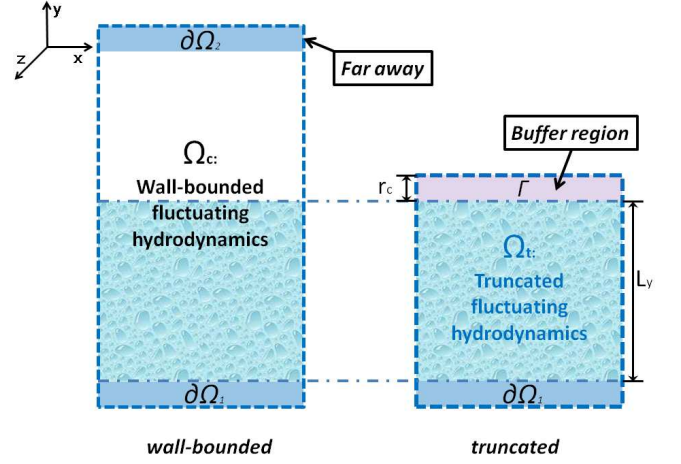

Figure 10: (Color online) Sketch of a single and complete wall-bounded simulation (left) versus a simulation in a truncated domain (right): in the left figure, the domain is bounded by two solid walls in the y direction; in the right figure, the domain is bounded by one solid wall at $y \leq 0$ and attached a buffer region Γ at $L_y \leq y \leq L_y + r_c$. Periodic boundary condition is applied in the other direction in both figures. Results in the two domains of length L_y are compared to each other.

is the Dirac delta function, as shown in Section III B, the velocity may be drawn from the known Gaussian distribution as shown in Fig. 2(a), that is, the Maxwell-Boltzmann distribution, in the buffer region Γ at every time step. However, the density of SDPD particles has a non-zero spatial correlation within r_c distance, as shown in Section III B. Therefore, the density field in the buffer region can not be simply drawn from the known Gaussian distribution as shown in Fig. 2(b). In fact, it should be given as a *conditional* Gaussian distribution taking into account its spatial correlation with interior particles below the Γ region. For this purpose, we introduce a Kriging method to provide such a conditional Gaussian distribution, which considers the available density distribution of the interior particles and preserves the spatial correlations of density.

A. Spherical model for the covariance and semivariance

Since we need to supply the semivariance (or covariance) to a Kriging method [44–46] in Section IV B, we select a spherical model to represent the semivariance of SDPD density

$$S(g) = sill \begin{cases} \left[1.5\left(\frac{g}{r_c'}\right) - 0.5\left(\frac{g}{r_c'}\right)^3\right], & 0 \leq g < r_c'; \\ 1, & g \geq r_c', \end{cases} \quad (24)$$

where $sill$ is defined as the plateau value at long distance. Given the simulation data (for $r_c = 0.15$, $\eta = 49.71$ and $c_T = 600$) in Sec. III B, the semivariance of SDPD density is shown in Fig. 11. The spherical model is better than other models, such as the exponential or Gaussian model [45, 47], as the former has a clearly defined sill, in line with the SDPD data, whereas the latter only have asymptotic plateaus. Thereafter, the covariance can be described as

$$C_v(g) = sill - S(g). \quad (25)$$

Both covariance versus lag distance (correlogram) and semivariance versus lag distance (semivariogram) are plotted in Fig. 11. Since we wish to capture both the most significant part (at short distance) of the semivariance data and the variance at long distance by the best fitting of Eq. (24), we make $sill = \sigma_\rho^2 \approx 2.4 \times 10^{-4}$
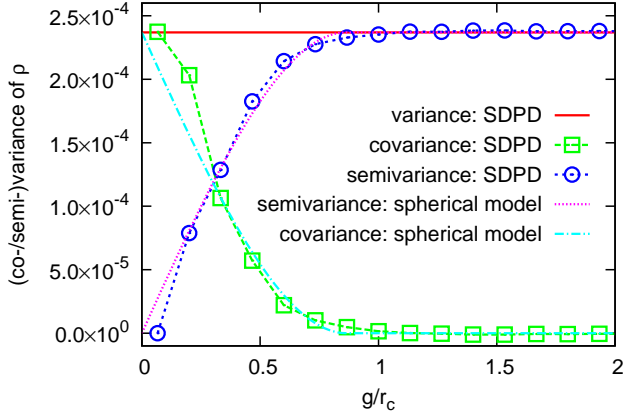
Figure 11: (Color online) Correlogram and semivariogram of SDPD density and their representations by a spherical model: simulation parameters are according to Sec. III A with $r_c = 0.15$ and $c_T = 600$.

Figure 12: (Color online) Sketch of a Kriging method for the density: particle A is in the buffer region Γ and its density is drawn from a *conditional* Gaussian distribution, which is solved by the Kriging method based on A's spatial covariance with the neighboring (blue) particles and the spatial covariance among themselves in the interior.

strictly, which is the variance of density, and further require that the lag distance g start from 0. Because the data are in discrete bins, e.g., the first bin is not exactly at $g = 0$, the best fit delivers $r'_c \approx 0.13$, which is slightly smaller than the SDPD cut off radius $r_c = 0.15$.

Eqs. (24) and (25) with selected *sill* and r'_c will be applied in the Kriging method presented in Section IV B.

B. Kriging method for density

A Kriging method can be understood as a variant of the basic linear regression estimator [45]. At a given simulation time step $t = n\Delta t$, the density value $\rho(\mathbf{x}_\alpha)$ of each SDPD particle in the interior is already calculated with full spherical support via Eq. (3). The estimation of the unknown density $\rho^*(\mathbf{x}_A)$ of any SDPD particle in the buffer region Γ can be defined as [44, 45],

$$\rho^*(\mathbf{x}_A) - \overline{\rho(\mathbf{x}_A)} = \sum_{\alpha=1}^{N_{krig}} \lambda_\alpha \left[\rho(\mathbf{x}_\alpha) - \overline{\rho(\mathbf{x}_\alpha)} \right], \quad (26)$$

where $\mathbf{x}_A$ and $\mathbf{x}_\alpha$ are the location vectors of a buffer particle and a neighboring particle in the interior (see Fig. 12). In particular, only the neighboring particles within r'_c distance away from $\mathbf{x}_A$ in the interior are considered, which is determined by the range of the spatial correlation length described in Fig. 11. Therefore, N_{krig} represents the number of interior particles, which are within r'_c away from the buffer particle at $\mathbf{x}_A$. $\overline{\rho(\mathbf{x}_A)}$ and $\overline{\rho(\mathbf{x}_\alpha)}$ are the expect values or means of $\rho(\mathbf{x}_A)$ and $\rho(\mathbf{x}_\alpha)$. It is easy to see that Eq. (26) estimates a residual component $R(\mathbf{x}_A) = \rho(\mathbf{x}_A) - \overline{\rho(\mathbf{x}_A)}$ at a location with unknown density. λ_α is the Kriging weight assigned to each $R(\mathbf{x}_\alpha) = \rho(\mathbf{x}_\alpha) - \overline{\rho(\mathbf{x}_\alpha)}$ and it is typically very different
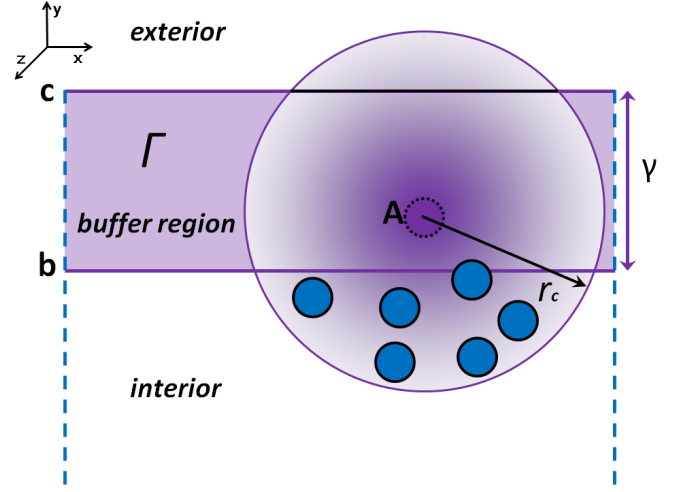
from the SPH kernel weight $W(\mathbf{x}_{A\alpha})$ in Section II, as the former considers explicitly the spatial correlation of the data while the latter has a fixed weight for a fixed distance. *The goal of Kriging is to determine the weights λ_α ($\alpha = 1, ..., N_{krig}$) that minimize the variance $\sigma^2(\mathbf{x}_A)$ between the estimation $\rho^*(\mathbf{x}_A)$ and the true value $\rho(\mathbf{x}_A)$*

$$\sigma^2(\mathbf{x}_A) = Var\left[\rho^*(\mathbf{x}_A) - \rho(\mathbf{x}_A)\right]$$
$$= \left\langle \left[\rho^*(\mathbf{x}_A) - \rho(\mathbf{x}_A)\right]^2 \right\rangle \quad (27)$$

under the unbiasedness constraint

$$E\left[\rho^*(\mathbf{x}_A) - \rho(\mathbf{x}_A)\right] = 0. \quad (28)$$

The random field $\rho(\mathbf{x})$ can be decomposed into residual and trend components, $\rho(\mathbf{x}) = R(\mathbf{x}) + \overline{\rho(\mathbf{x})}$, with the residual component treated as random field with a stationary mean of zero and a stationary covariance:

$$E\left[R(\mathbf{x})\right] = 0 \quad (29)$$
$$Cov\left[R(\mathbf{x}), R(\mathbf{x}+\mathbf{g})\right] = E\left[R(\mathbf{x}) \cdot R(\mathbf{x}+\mathbf{g})\right]$$
$$= C_v^R(\mathbf{g}). \quad (30)$$

$\mathbf{g}$ is the lag distance and the residual covariance function is generally derived from an input semivariogram model $S^R(\mathbf{g})$,

$$C_v^R(\mathbf{g}) = C_v^R(0) - S^R(\mathbf{g}) = sill^R - S^R(\mathbf{g}). \quad (31)$$

Since we are considering the simulation at equilibrium state in this work, the density field of a SDPD simulation is second-order stationary, which means that the mean and variance of $\rho(\mathbf{x})$ should be spatially invariant near the truncated region. Therefore, the estimation

is expected to be unbiased, since $E\left[\rho^*(\mathbf{x}_A) - \rho(\mathbf{x}_A)\right] = E\left[\rho^*(\mathbf{x}_A)\right] - E\left[\rho(\mathbf{x}_A)\right] = \rho_e - \rho_e = 0$, where ρ_e is the global mean value at equilibrium. Therefore,

$$\rho^*(\mathbf{x}_A) - \rho(\mathbf{x}_A) = [\rho^*(\mathbf{x}_A) - \rho_e] - [\rho(\mathbf{x}_A) - \rho_e]$$
$$= R^*(\mathbf{x}_A) - R(\mathbf{x}_A)$$
$$= \left[\sum_{\alpha=1}^{N_{krig}} \lambda_\alpha R(\mathbf{x}_\alpha)\right] - R(\mathbf{x}_A). \quad (32)$$

Using rules for the variance of a linear combination of random variables, the error variance of Eq. (27) becomes

$$\sigma^2(\mathbf{x}_A) = Var\left[R^*(\mathbf{x}_A)\right] + Var\left[R(\mathbf{x}_A)\right]$$
$$-2Cov\left[R^*(\mathbf{x}_A), R(\mathbf{x}_A)\right]$$
$$= \sum_{\alpha=1}^{N_{krig}} \sum_{\beta=1}^{N_{krig}} \lambda_\alpha \lambda_\beta C_v^R(\mathbf{x}_\alpha - \mathbf{x}_\beta) + C_v^R(0)$$
$$-2 \sum_{\alpha=1}^{N_{krig}} \lambda_\alpha C_v^R(\mathbf{x}_\alpha - \mathbf{x}_A). \quad (33)$$

To minimize the error variance, we take the derivative of the above expression to each unknown Kriging weight λ_α and set each derivative to zero. This leads to the following linear system of equations [44, 45]:

$$\sum_{\beta=1}^{N_{krig}} \lambda_\beta C_v^R(\mathbf{x}_1 - \mathbf{x}_\beta) = C_v^R(\mathbf{x}_1 - \mathbf{x}_A)$$

$$\sum_{\beta=1}^{N_{krig}} \lambda_\beta C_v^R(\mathbf{x}_2 - \mathbf{x}_\beta) = C_v^R(\mathbf{x}_2 - \mathbf{x}_A)$$

$$... = ...$$

$$\sum_{\beta=1}^{N_{krig}} \lambda_\beta C_v^R(\mathbf{x}_{N_{krig}} - \mathbf{x}_\beta) = C_v^R(\mathbf{x}_{N_{krig}} - \mathbf{x}_A). \quad (34)$$

Due to the spatially constant mean, the covariance for the residual is the same as for the random field, that is,

$$C_v^R(\mathbf{g}) = C_v(\mathbf{g}), \quad (35)$$

which is available from Eq. (25) by fitting SDPD density data beforehand via Eq. (24). Hence, Eq. (34) can also be written in a compact form as

$$\mathbf{K}\lambda = \mathbf{k}, \quad (36)$$

where each matrix element $\mathbf{K}_{ij} = C_v(\mathbf{x}_i - \mathbf{x}_j)$ is the density covariance between two interior particles, and each vector element $\mathbf{k}_i = C_v(\mathbf{x}_i - \mathbf{x}_A)$ is the density covariance between the buffer particle A and each interior particle. If there are no two interior particles located at the same position, which is true for SDPD particles due to the conservative force $\mathbf{F}_{ij}^C$, the matrix $\mathbf{K}$ is positive definite. Hence, the unknown Kriging weight vector is solved as
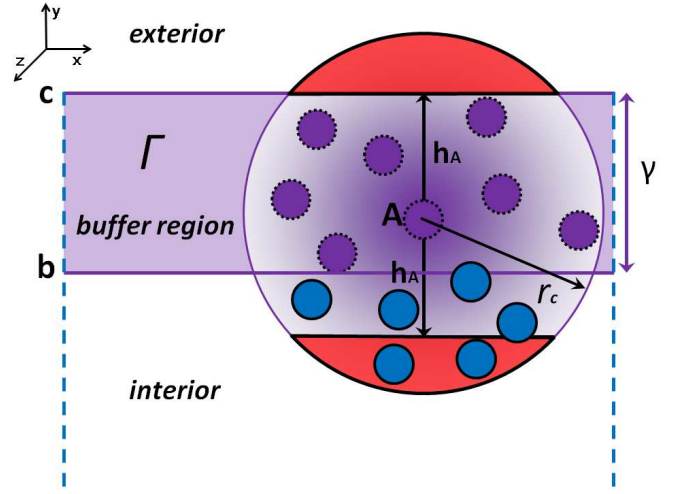
$$\lambda = \mathbf{K}^{-1}\mathbf{k}. \quad (37)$$

Figure 13: (Color online) Sketch of an asymmetric conservative force algorithm: particle A is in the buffer region Γ and its distance to the exterior (line c) is h_A. Since the upper segment of A's spherical region is in vacuum, the contribution from the opposite lower segment on the total conservative force of A along y direction is discarded.

For the relevance of a SDPD simulation in a truncated domain, it is only Eq. (37) that needs to be implemented to obtain λ. For a typical resolution $r_c = 3\Delta x$, $N_{krig} \lesssim 14$ in two dimensions, where the maximum number of Kriging neighbors is achieved when the interior neighboring particles occupy half of the spherical supporting volume of particle A. We simply apply the Gaussian elimination method to solve the small linear system of Eq. (37).

Once the Kriging weights λ are known, we can obtain both the estimated mean ρ_A from Eq. (26) and variance σ_A^2 from Eq. (33) for each particle A's density. The actual values of ρ_A and σ_A^2 are in general different from the global ρ_e and σ_e^2 measured from an equilibrium simulation in Section III A. Therefore, during the simulation, *the actual density of particle A in the buffer region is drawn from a Gaussian distribution with mean ρ_A and variance σ_A^2*. This Gaussian distribution is *conditional* in a sense that it must be determined by considering its spatial correlation with neighboring particles in the interior (vector $\mathbf{k}$) and also the spatial correlation within these particles themselves (matrix $\mathbf{K}$). All information to build $\mathbf{K}$ and $\mathbf{k}$ are local within cut off radius $r_c' \approx r_c$, therefore in the neighbor list of a SDPD implementation.

C. Asymmetric conservative force

For every particle A within the buffer region Γ, there is no full spherical support for calculating the conservative force $\mathbf{F}_A^C$ on the particle. This asymmetric particle distribution in the buffer region would lead to a large
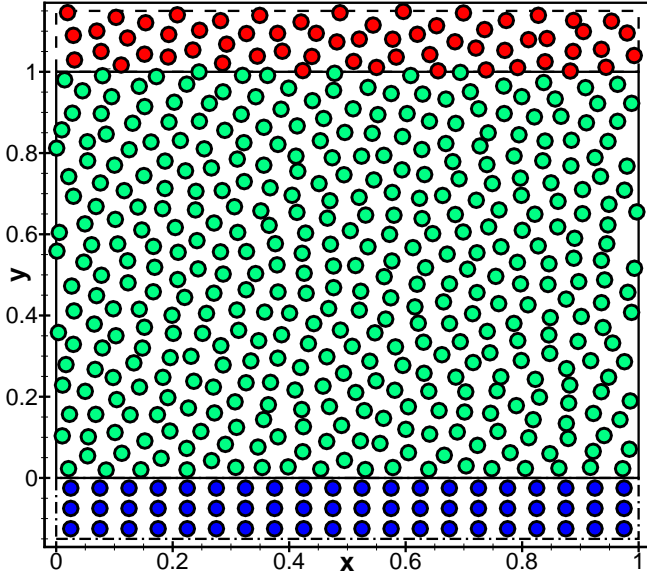
Figure 14: (Color online) An arbitrary snapshot of a truncated SDPD simulation: $r_c = 0.15$. Fluid region is between $y = [0, 1]$; wall region is between $y = [-0.15, 0]$; buffer region is between $y = [1, 1.15]$. A specular reflection is applied at $y = 1.15$.

pressure force on A towards the exterior. There exist a few methods, e.g., the "missing" force is represented by an integral of conservative force from an imagined region at exterior [25, 48]. However, these schemes are dependent on either the specific smoothing kernel or the RDF of particles at a particular set of parameters.

To compensate for the asymmetric conservative force and allow for dynamic change of pressure in the buffer region, we apply a simple conditional rule as follows, as sketched in Fig. 13, which was also previously applied in SPH simulations [33]. For every particle A within Γ and its neighboring particle B in the domain, their normal distances to the exterior boundary (horizontal line c in Fig. 13) are h_A and h_B; $\mathbf{F}_{AB}^C$ is their conservative force and F_{AB}^C is its magnitude. The tangential components, namely, $\mathbf{F}_{AB}^C \cdot \mathbf{e}_x$ remains unchanged between the two particles but the normal components are selected conditionally: *if $h_B \leq 2h_A$, $\mathbf{F}_{AB}^C \cdot \mathbf{e}_y$ is active for particle A; otherwise is discarded.* The main point of this rule is to satisfy that the sum of pairwise conservative forces on particle A from both sides along y direction are similar at equilibrium. The same rule applies to particle B: *if $h_A \leq 2h_B$, $\mathbf{F}_{BA}^C \cdot \mathbf{e}_y$ is active for particle B; otherwise is discarded.*

Due to the formulation adopted in Eq. (6), $\mathbf{F}_{AB}^C$ is repulsive between particles and always promotes regularization of particle configurations [41]. Therefore, the conditional rule also regularizes the particle distributions to facilitate the density calculation in the interior. We present an arbitrary snapshot of a simulation in the truncated domain in Fig. 14, where a regular distribution of

SDPD particles is maintained in both the interior and buffer regions.

Dissipative and random forces for the particles in the buffer region are calculated the same way as for the particles in the interior. To prevent particles from flying away, in the very end of the buffer region Γ, a specular reflection is applied inwards at line c in Fig. 13 or the same line at $y = 1.15$ in Fig. 14.

Technical details on all the operations designed for the truncated domain are elaborated according to the time integrator in Appendix B.

D. Simulation results

Based on the algorithms presented in Sections IV A, IV B, and IV C, we compute some statistics, spatial correlations and temporal correlations of truncated SDPD simulations. Furthermore, we shall compare the temporal correlations of truncated simulations with that of complete simulations in a single wall-bounded domain (see sketch in Fig. 10). The no-slip boundary condition at the fluid-solid interface is described in Appendix G. We pay close attention to the comparison of a Gaussian buffer and Kriging buffer at the end of the truncated domain. To avoid confusion, a Gaussian buffer means that both velocity and density of SDPD particles are drawn from known Gaussian distributions within Γ. A Kriging buffer means that velocity is drawn from a known Gaussian distribution, whereas density is drawn from a conditional Gaussian distribution provided by the Kriging method within Γ.

All simulations in a truncated domain presented in this section run with $r_c = 3\Delta x = 0.15$, $\eta = 49.71$, $c_T = 600$, and $\Delta t = 1.4 \times 10^{-5}$ within a box $\{0, L_x\} \times \{0, L_y\} = \{0, 1\} \times \{0, 1\}$. Solid wall region is located at $-r_c \leq y \leq 0$ and buffer region is placed at $L_y \leq y \leq L_y + r_c$. Results are ensemble-averaged over $N_s = 50$ independent runs.

1. Means and variances of density and velocity

We first examine the mean values of velocity and density across the truncated simulations along y direction and the results are shown in Fig. 15. We observe that the bin-averaged velocity is always zero across the channel and there is no difference on the performance between a Gaussian buffer and a Kriging buffer.

The bin-averaged density profiles are calculated by counting the *actual number* of particles located in each bin and dividing the bin's volume. We notice a slight deviation from the Gaussian buffer on the density profile in the last layer of interior, which is near the buffer region. A particle's density in the Gaussian buffer is drawn purely from a random Gaussian distribution without considering its spatial correlation with the interior neighboring particles. As a consequence, particles in the nearest interior layer feel a slight disturbance of pressure forces

Figure 16: (Color online) Temperature or velocity variance profile of truncated SDPD simulations: velocity data are bin-averaged quantities.
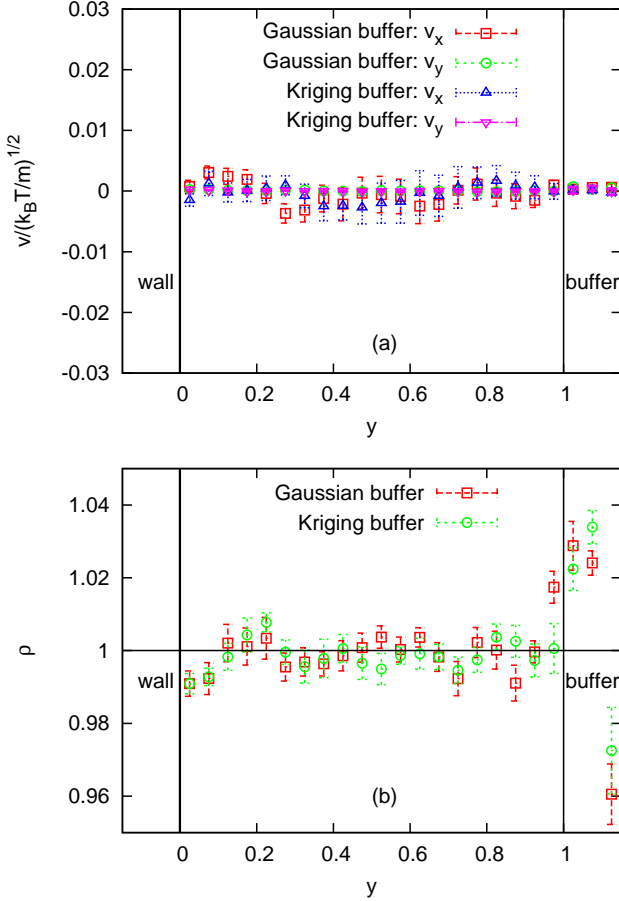

Figure 15: (Color online) Velocity and density mean profiles of truncated SDPD simulations. (a) velocity. (b) density. Velocity data are bin-averaged quantities and density data are bin-averaged by counting the actual number of particles.

It is interesting to note that if density profiles are calculated by bin-averaging the SDPD density of particles, instead of counting the actual number of particles as in Fig. 15, the disturbance of density mean profiles from the Gaussian buffer is smoothed out, due to the summation form in Eq. (3). Therefore, there is no difference for the SDPD density profiles between the Gaussian buffer and Kriging buffer, as shown in Fig. 17(a). In this case, we further examine the variance profile of the SDPD density. Despite the smooth property of SDPD density, we still observe that in the last layer of interior particle near the buffer region, the variance deviates $\sim 4\%$ for the Gaussian buffer while only $\sim 2\%$ for the Kriging buffer, as shown in Fig. 17(b).

2. Spatial correlation of density

We wish to verify if we preserve the spatial correlation of density in the truncated simulations and if the proposed Kriging method is effective. Therefore, we calculate the spatial correlation between each interior particle and each buffer particle and results are shown in Fig. 18. We observe that the Gaussian buffer does not consider spatial correlation at all, therefore it is not surprising to obtain the Dirac delta function. On the contrary, the Kriging buffer explicitly considers the spatial correlation between buffer particles and interior particles, and as a result, the measured spatial correlation recovers the actual spatial correlation measured in periodic domains in Section III B. A slight deviation of Kriging buffer from periodic domains is due to the error of representing the actual data covariance with the spherical model in Section IV A. We may conclude that the proposed Kriging method is effective in preserving a given spatial correlation of density between SDPD particles.

from the buffer, which cause a small jump ($\sim 2\%$) of the density profile. On the contrary, each particle's density in the Kriging buffer is drawn from a conditional Gaussian distribution, which respects its spatial correlation with the interior neighboring particles. As a result, the density profile is unaffected for the interior layer near the Kriging buffer region. Both density profiles inside the Gaussian buffer and Kriging buffer deviate ($\lesssim 4\%$) from unity, due to the specular reflection applied at the end of the domain ($y = L_y + r_c$). *However, the data in buffer regions are only auxiliary, i.e., the results obtained there are dispensable.*

We further assess the temperature profile in each direction, which is defined as the average kinetic energy of particles in that direction. Since the velocity means are zero at equilibrium and the temperature so defined also indicates the variance of velocity distribution. Results are shown in Fig. 16, where both the Gaussian and Kriging buffer deliver good temperature profiles, in agreement with the input temperature.
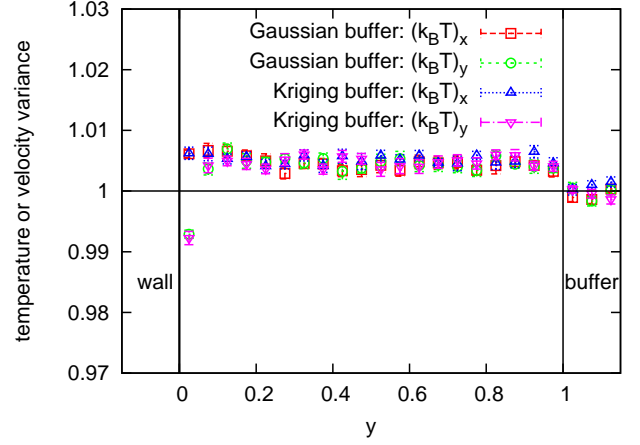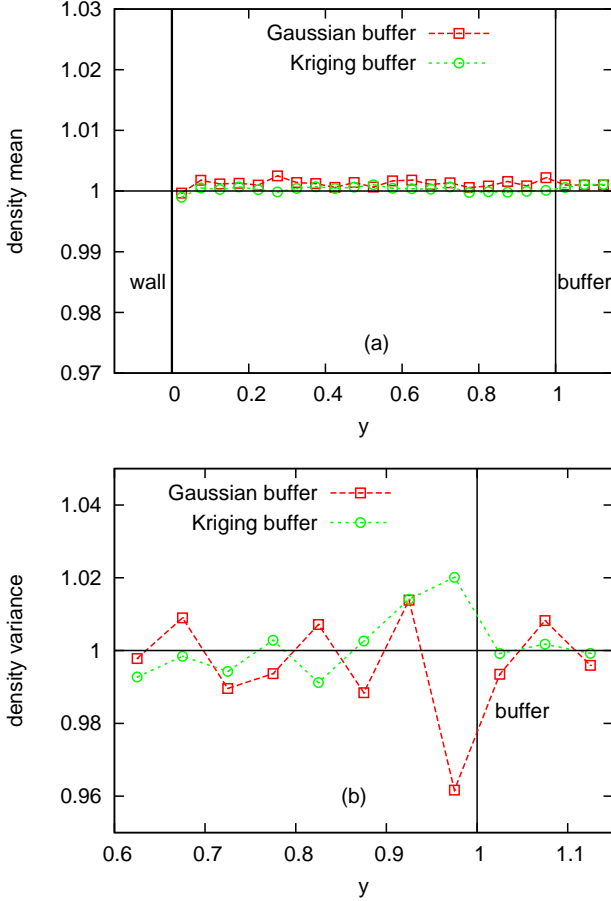
Figure 17: (Color online) Density mean and variance of truncated SDPD simulations. (a) mean. (b) variance. Density data are bin-averaged from the SDPD density of particles. Density variance is normalized by the variance measured in the periodic domains presented in Section III A.
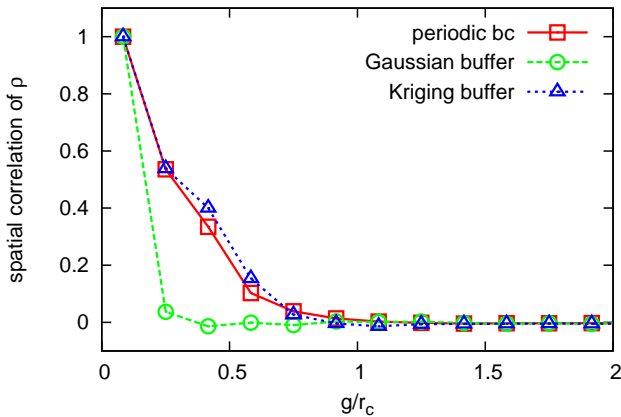

Figure 18: (Color online) Spatial correlation of density between SDPD particles in the buffer and interior regions: Gaussian buffer and Kriging buffer versus simulations in periodic domains.

3. Temporal correlations

In this section, we examine the error committed on temporal CFs by the truncated simulations. Therefore, we take a complete wall-bounded simulation as the reference solutions, as sketched in Fig. 10, where the temporal correlations on the shadowed regions will be compared with each other.

Before the actual evaluation of the truncated simulations, we establish some baselines of simulation results in a wall-bounded domain by comparing its CFs with that of simulations in a periodic domain, as presented in Section III C. We run wall-bounded simulations in a box of $[L_x, 4L_y] = [1, 4]$ and two solid wall regions are located at $-r_c \leq y \leq 0$ and $L_y \leq y \leq L_y + r_c$, respectively. We take wave vectors as $\mathbf{k} = (k, 0)$ in x-direction, which is periodic. In particular, we calculate CFs within the shadowed region $\{0, 1\} \times \{0, 1\}$, as shown in Fig. 10, and consider only one wave number $k = 1 \times 2\pi/L_x$. We present the transversal and longitudinal ACFs, and longitudinal-density CCFs in Fig. 19. After time is rescaled by νk^2, we observe that the transversal ACF for the wall bounded domain decays much faster than that of the periodic domain, as shown in Fig. 19(a). As the transversal ACF is purely determined by the shear mode, this indicates that the dissipation is much stronger in y direction for wall bounded simulations, due to the presence of the wall. By rescaling the time by $c_T k$, we observe that the longitudinal ACF and longitudinal-density CCF for the wall bounded domain decay faster than that of the periodic domain, as shown in Fig. 19(b) and 19(c), indicating that sound attenuation is enhanced along x direction due to the presence of the wall. Nevertheless, the oscillating periods in Fig. 19(b) and 19(c) are not altered, indicating the same sound speed traveling in x direction for both simulations.

We also compare two sets (each consist of $N_s = 50$ independent runs) of wall-bounded simulations in a box of $[L_x, L_y] = [1, 2]$ and $[L_x, L_y] = [1, 4]$ and observe no apparent difference on the CFs in the shadowed regions ($\{0, 1\} \times \{0, 1\}$). Therefore, the solutions for the shadowed region from box $[L_x, L_y] = [1, 4]$ will be taken as the reference solutions.

After learning the characteristics of CFs in wall-bounded simulations, we proceed to compare the truncated simulations with wall-bounded simulations. We always take wave vectors as $\mathbf{k} = (k, 0)$ in the x-direction. In particular, we focus on two wave numbers, that is, $k = 2\pi n_w/L_x$ with $n_w = 1$ and 2, and examine the CFs in length scales 1 (box length in x direction) and 0.5.

On the large scale with $k = 2\pi/L_x$, both the Gaussian and Kriging buffers lead to stronger dissipations in y direction, which is indicated by the faster decay on transversal ACF than that of the wall-bounded complete simulations, as shown in Fig. 20(a). On the small scale with $k = 4\pi/L_x$, the dissipation along y direction is not affected by either the Kriging or the Gaussian buffer, as shown in Fig. 20(b).
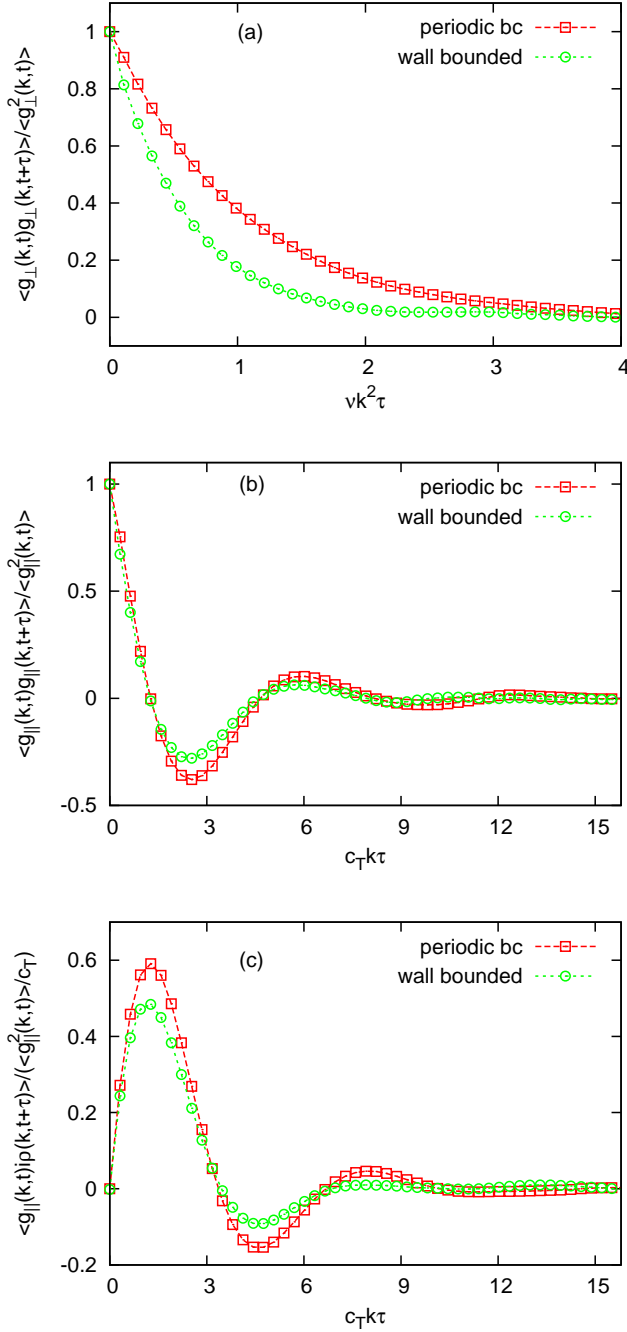
Figure 19: (Color online) Correlations of wall-bounded domain versus that of periodic domain. (a) transversal. (b) longitudinal. (c) longitudinal-density. Wave vector $\mathbf{k} = (k, 0)$ in x direction and $k = 2\pi/L_x$.
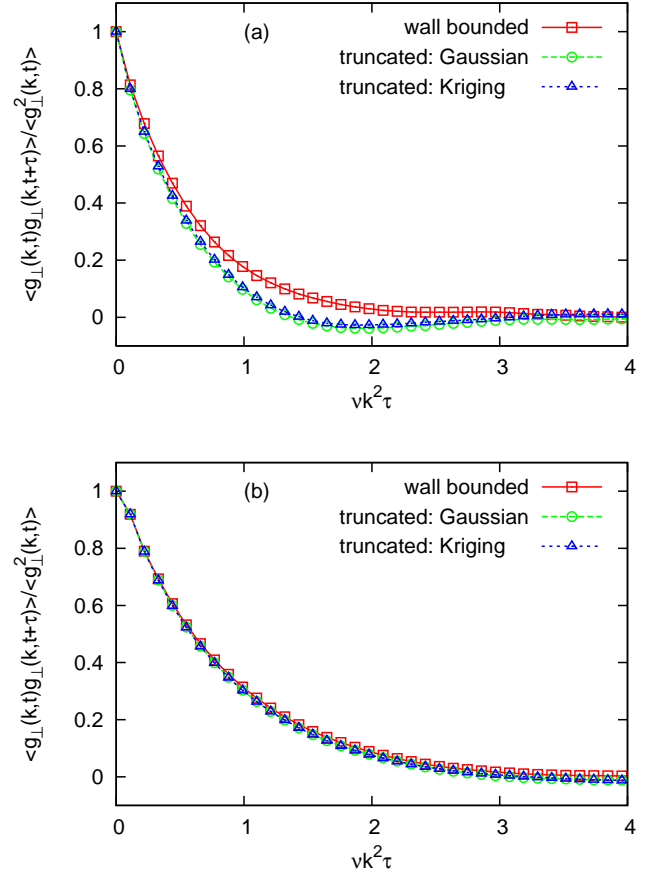

Figure 20: (Color online) Transversal autocorrelations of truncated SDPD simulations versus that of wall-bounded simulations. (a) $k = 1 \times 2\pi/L_x$. (b) $k = 2 \times 2\pi/L_x$. Wave vector $\mathbf{k} = (k, 0)$ in x direction.

uation along x direction at large scale with $k = 2\pi/L_x$, as shown in Fig. 21(a).

We may reduce the extra attenuation and dissipation along x and y direction, respectively, by introducing a gap region as a "buffer" region of the buffer, which is sketched in Fig. 22. By gradually increasing the height of the gap region, the extra attenuation and dissipation are reduced to only a small residual for $r_{gap} = r_c$, as shown in Fig. 23. Although results are shown for the Kriging buffer, the behavior of the Gaussian buffer is quite similar.

V. DISCUSSIONS AND CONCLUSIONS

We implemented the smoothed dissipative particle dynamics (SDPD) method to study fluctuating hydrodynamics (FH) in both periodic domains and truncated domains in the context of multiscale coupling via the domain decomposition (DD) method. The derivation of the standard SDPD method adopts a smoothed particle hy-

Furthermore, from the oscillations of CCFs, neither the Gaussian buffer nor the Kriging buffer alters the sound speed along x direction, if compared to the complete wall-bounded simulations, as shown in Fig. 21. However, the presence of either the Gaussian buffer or the Kriging buffer indeed enhances slightly the sound atten-
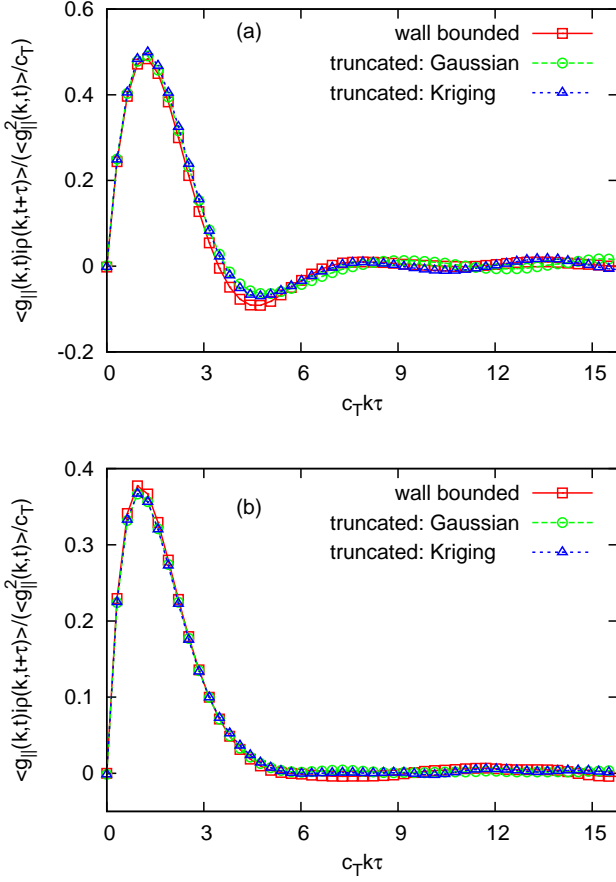
Figure 21: (Color online) Longitudinal-density correlations of truncated SDPD simulations versus that of wall-bounded simulations. (a) $k = 1 \times 2\pi/L_x$. (b) $k = 2 \times 2\pi/L_x$. Wave vector $\mathbf{k} = (k, 0)$ in x direction.
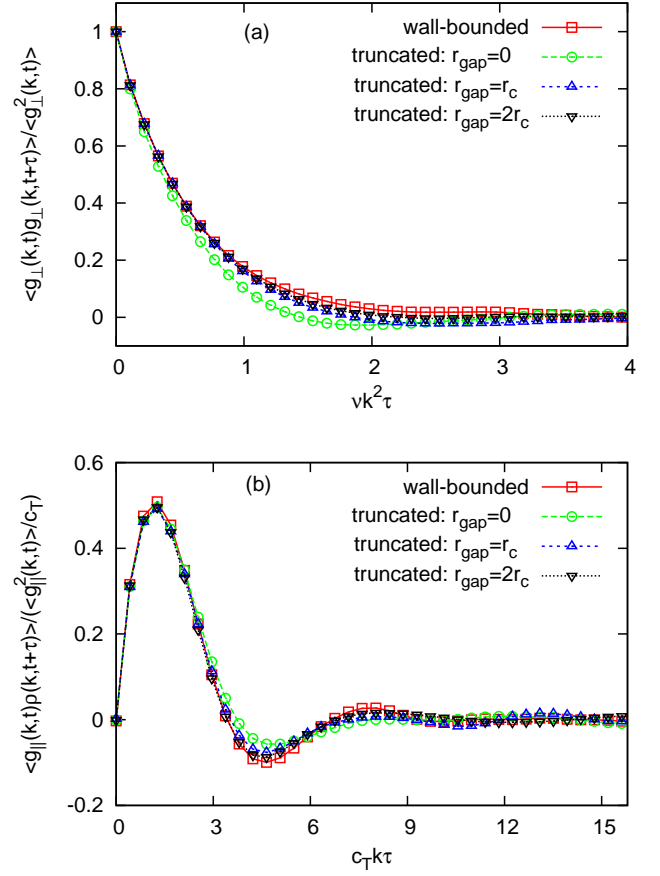

Figure 23: (Color online) Effects of the gap region between the Kriging buffer and interior on the correlation functions. (a) transversal. (b) longitudinal-density. Wave vector $\mathbf{k} = (k, 0)$ in x direction and $k = 2\pi/L_x$.
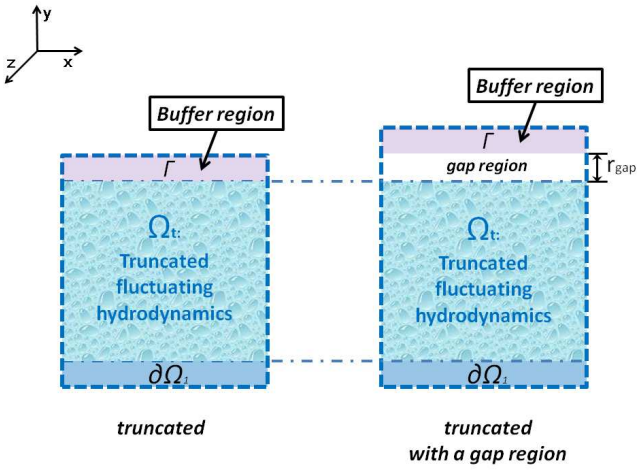

Figure 22: (Color online) Sketch of a truncated domain with a gap region between the artificial buffer and interior.

drodynamics (SPH) discretization of the Navier-Stokes (NS) equations, to obtain the pairwise conservative and dissipative forces between particles. To guarantee the thermodynamical consistency in actual simulations, the pairwise random force is introduced *directly* on the discrete particle level within the GENERIC framework, and the final SDPD formulation is obtained. Hence, SDPD does not discretize directly the FH described by the Landau-Lifshitz Navier-Stokes (LLNS) equations [1], although it was proposed as the discrete version of the FH [9].

To identify *explicitly* the one-to-one correspondence between SDPD and the FH theory, we computed probability distributions, spatial correlations, and temporal correlations of the random state variables of SDPD simulations in periodic domains. We confirmed that the statistics for velocity and density of SDPD particles agree well with that of well-known distributions. We further found that the spatial correlation for the velocity of SDPD particles is the Dirac delta function, as predicted by the

theory. However, the density of SDPD particles has spatial correlation within finite range r_c, which is the cut off radius of the method, in contradict to the Dirac delta function from the theory. This range of correlation is inevitable, if the density summation form of SPH in Eq. (3) is applied, which considers mutual contributions among neighboring particles within r_c distance. Nevertheless, the finite range of spatial correlation can be reduced to an arbitrarily small value by decreasing the r_c, which is how the smoothing kernel converges to the Dirac delta function in Eq. (5).

We emphasize that the discrepancy between the SDPD simulation and the FH theory on density spatial correlation should not be confused with the kernel approximation error of the SPH method, which is in the order of $O(h^2)$ [35, 41]. Perhaps the finite range of spatial correlation on density may be avoided, if the continuity equation is solved directly by SPH [35]. To have both variational and thermodynamic consistencies [9, 36], however, the conservative forces must be modified according to the density calculation. This type of modification on the original SDPD formulation definitely needs further elaboration before a definite conclusion is drawn. Therefore, for all simulations performed we preferred the density summation form adopted in the original SDPD formulation.

In the linear regime, where both v_T and $\delta\rho/\rho_e$ are very small, we have calculated the temporal correlation functions (CFs) of SDPD random field variables in Fourier space. In particular, we performed SDPD simulations in periodic domains and examined the autocorrelation functions (ACFs) of transversal and longitudinal components of momentum density, and further ACF of the density and cross correlation functions (CCFs) between longitudinal momentum and density. We observed an overall good agreement between simulations and the analytical solutions of the linearized FH. At large wave number k, ~ 10 particles per wavelength, however, we found small deviations between the SDPD results and the analytical solutions. One could still fit the simulation results with wave-number dependent viscosity and sound speed [19, 20], instead of the constant input ones for the simulations. However, such an approach is inappropriate, as SDPD is a top-down approach based on the continuum assumption. Therefore, the discrepancy at large wave number should be interpreted as numerical error due to the insufficient numerical resolution of the method. On the contrary, both the transport coefficients and the sound speed of DPD method may have wave-number dependency. This should be analyzed by the generalized fluctuating hydrodynamics, as it has both collective regime and particle regime similarly as in molecular dynamics. In order not to digress from the main subject, we have only reported the continuum behavior in the linear regime for DPD in Appendix F. The measurement of ACFs also suggests an alternative means of extracting viscosities and sound speed of a DPD system with a new set of input parameters.

From the assessments in periodic domains, we considered the SDPD method as an effective solver for the FH and applied it in truncated domains. This is a specific scenario in the context of multiscale coupling of heterogeneous adjacent multi-domains via the domain decomposition (DD) method. In this context, a SDPD simulation is assumed to be coupled with a Naiver-Stokes (NS) solver, such as the finite volume method, the SPH, or the spectral element method. In contrast to the majority of the past research, where nonequilibrium flows were simulated and the mean velocity profiles were reported, we focused on the equilibrium state to assess closely the thermal fluctuations. To this end, we did not actually perform any NS simulations, since the means of field variables (e.g., velocity and density) are known *a priori*. Therefore, we modeled a buffer region Γ as an equilibrium boundary condition (EBC) at the truncated side of SDPD simulations, which was supposed to be coupled with a NS solver. Moreover, we applied a solid wall at the other side of the truncated domain to confine the system.

We have implemented two types of buffers for the EBC. The first is the Gaussian buffer, where both velocity and density of SDPD particles were drawn from known Gaussian distributions at each time step. The second is the Kriging buffer, where velocity is drawn from the known Gaussian distribution, whereas density is drawn from a *conditional* Gaussian distribution at each time step. The density distribution in Γ is conditional in the sense that it considers its spatial correlation with interior neighboring particles and the spatial correlations among themselves. We have introduced and implemented the Kriging method, which considers the covariance of available density data represented by the spherical model. Once the interior densities of SDPD particles are calculated by the SPH kernel summation at each time step, the density distribution of a buffer particle is provided by solving a small linear system of equations. As a result, the estimated distribution of density has the minimum variance. The computational cost of the Kriging method is negligible due to two observations: i) it is needed only near the buffer region locally. ii) the information for building up the Kriging matrix and vector are all within the range of r_c (SDPD cut off radius) away from the estimated location.

We observed that the Gaussian buffer disturbs the mean and variance of density in the nearest layer of interior, whereas the disturbance of the Kriging buffer is negligible. More importantly, the Kriging buffer preserves the spatial correlation of density between particles in the buffer region and the interior, consistently with the properties of SDPD in periodic domains, whereas the Gaussian buffer completely ignores any finite spatial correlation within a finite range.

Finally, we evaluated the temporal CFs of the SDPD simulations in the truncated domains by comparing with complete simulations at the same region in a single wall-bounded domain. We observed that both Gaussian buffer and Kriging buffer for the EBC maintain the correct

sound speed at all length scales along the periodic direction. *However, at large length scale both buffers cause an extra amount of dissipation in the direction perpendicular to the wall and an enhanced sound attenuation along the periodic direction.* For the viscous fluids simulated, the relaxation time τ_{vv} of the velocity field is very short but not zero; for example, the velocity autocorrelation (VACF) of a SDPD particle in physical space decays to zero within ~ 10 time steps. By assigning the velocity in the buffer region with a purely *white noise* at each time step, we introduced artificially such an extra dissipation. This is also how most of the multiscale coupling schemes do, to assign values to the underdetermined degrees of freedom on the fine scale side. To faithfully model the buffer region Γ, a *colored noise* would be a better approach to generate the actual velocity of particles at each time step by respecting the short memory of the VACF. However, this approach would be computationally expensive. As a way around it, we adopted a much simpler strategy, where we introduced a small gap region as the "buffer" of the buffer region Γ, so that the extra dissipation in the interior can be minimized. The positive influence of the gap region may be understood by the fact that the extra dissipation introduced by neglecting the ~ 10 time steps memory diffuses and fades out over r_c distance. The gap region between the artificial buffer and the interior would be definitely necessary for the nonequilibrium simulations, if not more important than the equilibrium case considered here, to minimize any artificial dissipation caused by a multiscale coupling algorithm. The fluctuating properties in multiscale coupling for nonequilibrium flows are currently under investigation.

The Kriging buffer introduced indeed preserves effectively the intended spatial correlation between particle densities, but it has no observable better effects on the CFs than the simple Gaussian buffer. We expect that the Kriging method may play a more important role at nonequilibrium, where both density and velocity have spatial correlations.

Finally, we point out that we could not quantify the errors of the sound speed along the y direction perpendicular to the wall in the truncated domains, as the wave vectors were selected only in the periodic x direction, due to the periodic basis functions of Fourier analysis. Probably other non-periodic basis, such as the Legendre and Chebyshev polynomials, may be adopted to define the wave vector in y direction, to further compare extensively the fluctuating properties of FH simulations in a truncated domain and that in a single complete wall-bounded domain. Another relevant work along this research direction has been reported in the context of a grid-based method [49]. In future, we will work on accurate sound propagation across different scales.

Appendix A: Quintic spline of SPH

In this work the quintic kernel from the B-spline family is adopted, which has been widely utilized since the inception of SPH simulation for viscous flows [37]:

$$W(s) = c_D \begin{cases} (3-s)^5 - 6(2-s)^5 + 15(1-s)^5, & 0 \le s < 1; \\ (3-s)^5 - 6(2-s)^5, & 1 \le s < 2; \\ (3-s)^5, & 2 \le s < 3; \\ 0, & s \ge 3, \end{cases} \tag{A1}$$

where $s = 3r_{ij}/r_c = r_{ij}/h$ and r_c is a finite cut off radius based on user's choice to control numerical errors. The normalization coefficients are $c_2 = 63/(478\pi r_c{}^2)$ and $c_3 = 81/(360\pi r_c{}^3)$ in two and three dimensions, respectively.

Appendix B: Time integration and operation order for simulations in truncated domain

In this work, we apply the velocity Verlet integrator [7, 19] for each SDPD particle i as,

$$\tilde{\mathbf{v}}_i(t) = \mathbf{v}_i(t - \Delta t) + \frac{1}{2}\Delta t \mathbf{f}_i(t - \Delta t), \tag{B1a}$$

$$\mathbf{r}_i(t) = \mathbf{r}_i(t - \Delta t) + \Delta t \tilde{\mathbf{v}}_i(t), \tag{B1b}$$

$$d_i(t) = \sum_j W[\mathbf{r}_{ij}(t)], \tag{B1c}$$

$$\mathbf{f}_i(t) = \mathbf{f}[\mathbf{r}_{ij}(t), d_i(t), d_j(t), \tilde{\mathbf{v}}_{ij}(t)], \tag{B1d}$$

$$\mathbf{v}_i(t) = \tilde{\mathbf{v}}_i(t) + \frac{1}{2}\Delta t \mathbf{f}_i(t), \tag{B1e}$$

where $\mathbf{f}_i$ is the total force per unit mass on particle i.

In the case of SDPD simulations in a truncated domain, we elaborate on some distinct operations on particles in the buffer region according to the time integration. Eqs. (B1a)(B1b) (B1d)(B1e) all apply to buffer particles, which makes the buffer particles still Lagrangian.

Eq. (B1c) does not apply to buffer particles. For the Kriging buffer (with the conditional Gaussian distribution as described in section IV B), density for each buffer particle is calculated by solving a small matrix to obtain the kriging weights in Eq. (37). Immediately after Eq. (B1c), when the densities for all interior particles are already available, density of each buffer particle is drawn from a Gaussian distribution with mean and variance described by Eqs. (26) and (33), respectively. For the Gaussian buffer, density for each buffer particle is

drawn randomly/unconditionally from a known Gaussian distribution evaluated within a periodic domain.

At the end of each time step, that is, after Eq. (B1e), for both the Kriging and Gaussian buffers velocity for each buffer particle is "shuffled" randomly/unconditionally from a known Gaussian (the Maxwell-Boltzmann) distribution at the given temperature.

The asymmetric operation (described in section IV C) on conservative force of each buffer particle is performed at the stage of Eq. (B1d) at time t, which will reflect its effects at the stage of Eqs. (B1a)(B1b) at time $t + \Delta t$, to regulate the particle distribution in the buffer region. After updating the position in Eq. (B1b), if a buffer particle leaves the buffer region towards to the exterior, which is very rare due to the asymmetric conservative force, a specular reflection is performed at the external end of the buffer region.

Appendix C: Quantile-Quantile plot

To explicitly verify that the PDFs of velocity and density for SDPD particles are indeed Gaussian functions with symmetric distributions, we present the quantile-quantile (Q-Q) plot for both quantities in Fig. 24. In Fig. 24(a), the sorted velocity values are shown against the standard normal quantiles of the Maxwell-Boltzmann distribution, while in Fig. 24(b) the sorted density values are plotted against the standard normal quantiles of a fitted Gaussian function of Fig. 2(b). We observe that both Q-Q plots on in Fig. 24 have clearly linear slopes, which indicate a negligible skewness on the PDFs of Fig. 2.

Appendix D: Effective equation of state

We apply the virial theorem of Clausius [7, 19] to calculate the effective pressure of our SDPD simulations

$$\mathbf{P} = dk_BT + \frac{1}{3V}\sum_{i=1}^{N}\mathbf{r}_i \cdot \mathbf{F}_i, \qquad (D1)$$

where $\mathbf{F}_i$ is the total force on each particle i. Thereafter, we compare the effective equation of state against the input one in Fig. 25, where we obtain a good agreement between the intended equation of state and the effective one for the parameter range studied ($r_c = 0.15$, $\eta = 49.71$ and $c_T = 300 - 1500$).

Appendix E: Numerical error and hierarchy of time scales

The numerical error shown in Fig. 9(b) is due to the inappropriate choice of the SDPD parameters, that is,
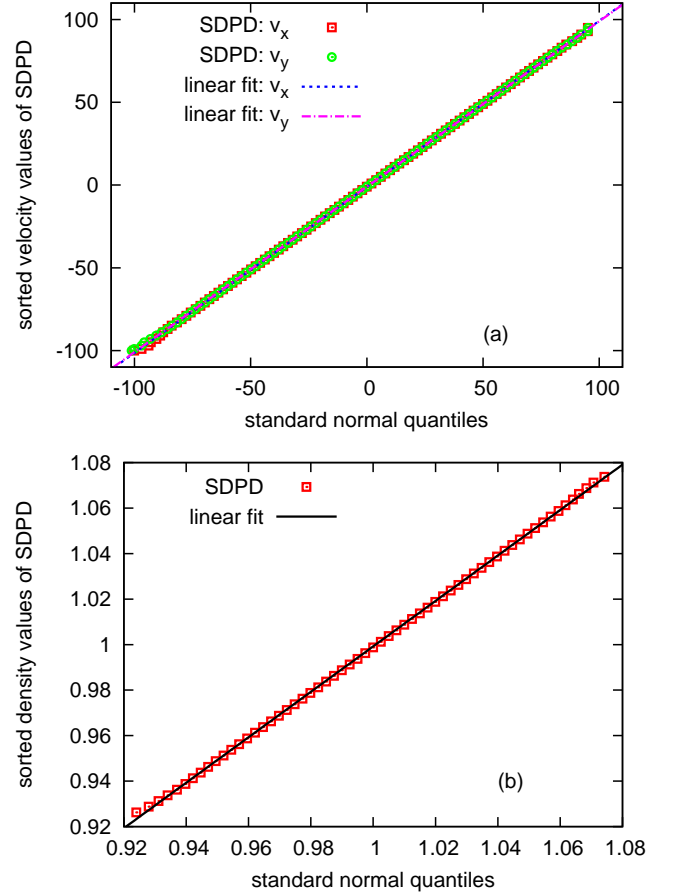

Figure 24: (Color online) Quantile-quantile (Q-Q) plot for velocity and density of SDPD particles. (a) velocity: the standard normal quantiles are obtained from the Maxwell-Boltzmann distribution. (b) density: the standard normal quantiles are obtained from a fitted Gaussian distribution.
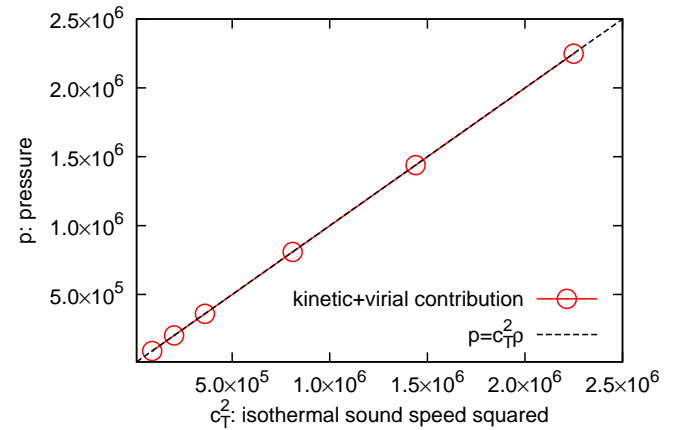

Figure 25: (Color online) The effective equation of state (EOS) versus model EOS.

c_T	τ_ν/τ_c
300	0.9
450	1.4
600	1.8
900	2.7
1200	3.6
1500	4.5

Table I: Time scale ratios at different isothermal sound speeds: $r_c = 0.15$ and $\nu = 49.71$. $\tau_c = r_c/c_T$ and $\tau_\nu = r_c^2/\nu$.

$c_T = 300$ is too small for a correct weakly compressible description [35, 37, 38].

Rather than a rigorously numerical analysis for the stochastic SDPD system, probably it is relatively simpler to interpret the numerical error by considering the characteristic times scales of SDPD particles. For the weakly compressible fluids considered here, the sonic and viscous time scales may be defined as $\tau_c = l/c_T$ and $\tau_\nu = l^2/\nu$, where l is a characteristic length scale. The ratio of the two time scales is $\gamma = \tau_\nu/\tau_c = lc_T/\nu$. For a typical liquid at continuum length scale, it should be $\gamma >> 1$ for the correct physics to emerge [50]. For example, for water at ambient condition, $\gamma \sim O(1)$ only when $l < 10^{-9}m$. For the SDPD simulations considered in this work ($\nu = \eta/\rho = 49.71$), if we take $l = r_c = 0.15$, $\tau_c = r_c/c_T$ and $\tau_\nu = r_c^2/\nu$, the ratios of the two time scales at different isothermal sound speeds are given in Table I. For a defined length scale r_c, with decreasing c_T the viscous effect may propagate at similar or even faster speed than the sound wave. Therefore, the dynamic behaviors (e.g., the longitudinal ACF shown in Fig. 9(b)) of particles are erroneously simulated, although the static properties such as pressure in Appendix D are correct. This heuristic argument may explain why the deviation of SDPD simulation with $c_T = 300$ in Fig. 9(b) is apparent.

To support this argument, we fix $c_T = 300$ and reduce viscosity to be $\nu = 12.43$. This makes $\tau_\nu/\tau_c = 3.6$, which is the same time ratio as for $c_T = 1200$ and $\nu = 49.71$. The longitudinal ACF for $c_T = 300$ and $\nu = 12.43$ is shown in Fig. 26, where agreement between SDPD simulation and the analytical solution is apparently recovered.

Appendix F: Temporal correlations of DPD

When input parameters of DPD are selected carefully, the temporal autocorrelation functions (ACFs) for DPD particles also agree well with the solutions of the linearized FH.

We consider the classical dissipative particle dynamics (DPD) method, which has three pairwise forces described
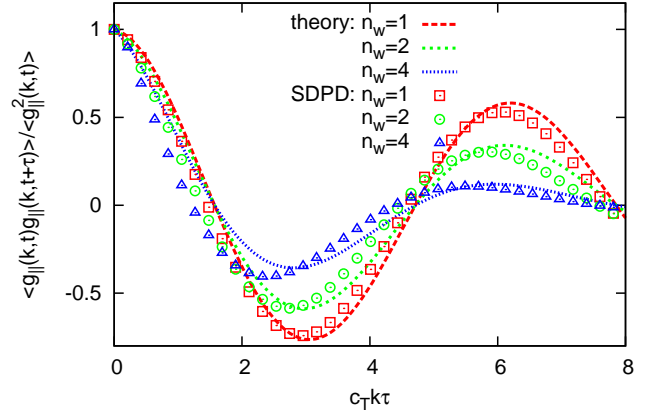

Figure 26: (Color online) Longitudinal ACF of SDPD simulations with $c_T = 300$ and $\nu = 12.43$.

as follows [6, 7]

$$\mathbf{F}_{ij}^C = aW^C(r_{ij})\mathbf{e}_{ij}, \qquad (F1)$$

$$\mathbf{F}_{ij}^D = -\gamma W^D(r_{ij})(\mathbf{e}_{ij} \cdot \mathbf{v}_{ij})\mathbf{e}_{ij}, \qquad (F2)$$

$$\mathbf{F}_{ij}^R = \sigma W^R(r_{ij})\theta_{ij}\mathbf{e}_{ij}\Delta t^{-1/2}, \qquad (F3)$$

where coefficients a, γ, and σ reflect the strength of individual forces; W^C, W^D, and W^R are weighting functions that monotonically decay with relative distance r_{ij}; $\theta_{ij} = \theta_{ji}$ is a Gaussian white noise with

$$< \theta_{ij}(t) > = 0, \qquad (F4)$$

$$< \theta_{ij}(t)\theta_{kl}(t') > = (\delta_{ik}\delta_{jl} + \delta_{il}\delta_{jk})\,\delta(t - t'), \quad (F5)$$

where δ_{ij} is the Kronecker delta and $\delta(t-t')$ is the Dirac delta function. The DPD version of the fluctuation-dissipation theorem (FDT) reads as [6]

$$W^D(r_{ij}) = \left[W^R(r_{ij})\right]^2, \qquad (F6)$$

$$2k_BT\gamma = \sigma^2. \qquad (F7)$$

A typical form of the weighting kernel is suggested as

$$W^{C,R}(r_{ij}) = \begin{cases} (1 - r_{ij}/r_c), & r_{ij} < r_c, \\ 0, & r_{ij} \geq r_c. \end{cases} \qquad (F8)$$

Following Refs. [7, 51], we take $\alpha = 18.75$, $\gamma = 4.5$, $\sigma = 3$, $m = 1$, number density $d = 4$, $k_BT = 1$, $\Delta t = 0.01$, $r_c = 1$ and a periodic box with size $[10L_x, 10L_y, 10L_z] = [10, 10, 10]$. We perform 20 independent simulations and obtain average of all initial conditions and meanwhile apply the same procedure introduced in Section III C to analyze DPD simulations. Since DPD does not have explicit density fields defined, we calculated its ACFs with velocity instead of momentum density,

$$\frac{< v_\perp(k,t)v_\perp(k,t+\tau) >}{\sigma^2[v_\perp(k,t)]} = e^{-\nu k^2\tau}. \qquad (F9)$$

For the transversal ACF, this substitution has no effect, since the shear mode is decoupled from the density. In particular, we consider one wave number $k = 2\pi/(10L_x)$ for the largest wavelength available. We present the transversal ACF in Fig. 27(a). We observe that the dissipation of DPD at length scale 10 has an exponential decay and follows the theory very well. The theory is according to the right hand side of Eq. (F9) with shear viscosity taken from a previous work [51], which is measured as $\eta = 1.077$ and $\nu = \eta/(md) = 0.26925$.

For the longitudinal ACF of DPD, it is defined as

$$\frac{< v_{||}(k,t)v_{||}(k,t+\tau) >}{\sigma^2 \left[v_{||}(k,t) \right]} = e^{-\Gamma_T k^2 \tau} cos(c_T k \tau), \quad \text{(F10)}$$

which is still a good approximation to Eq. (21b) for the DPD fluid considered here. To support the validity of the approximation, we show the ACF of longitudinal component in Fig. 27(b), which clearly has both damping and oscillating elements. In addition, we observe that the classical DPD method has both shear dynamic viscosity η and bulk viscosity ζ, in line with previous theoretical work [7, 52]. Hence, the solution of the longitudinal ACF needs to include also the (kinematic) bulk viscosity ζ and the isothermal sound absorption coefficient is now defined as $\Gamma_T = (4\eta/3 + \zeta)/(2md)$. With available η and the decaying rate on Fig. 27(b), we find that the bulk viscosity $\zeta \approx 2\eta/3 = 0.718$. Furthermore, from the oscillation period, we fit the isothermal sound speed to be $c_T = 4.085$, which corroborates the previous work [7, 52].

For practical users of DPD methods, this analysis also provides an effective means to extract viscosities and sound speed, or check the compressibility of a DPD system with a new set of input parameters. This approach has advantages over the wall-bounded or reversible Poiseuille flow method [51, 53], as the latter approaches need external perturbations and provide only shear viscosity. Furthermore, this measurement is also more convenient and efficient to infer the sound speed compared to previous work. For example, in Ref. [7], to obtain the sound speed, pressures at different density states have to be computed before calculating the slope of pressure variation with respect to density.

Finally, we note that the SDPD method is a top-down approach, which should only have a collective regime including deterministic hydrodynamics (as SPH method in the limit of zero fluctuations) and fluctuating hydrodynamics at mesoscale. On the contrary, a complete analysis of DPD method should consider both collective and particle regimes with wave-number dependence [19, 20], as it has both hydrodynamic behavior for simple/complex fluids [7] and discrete coarse-grained correspondence for complex fluids [54, 55].
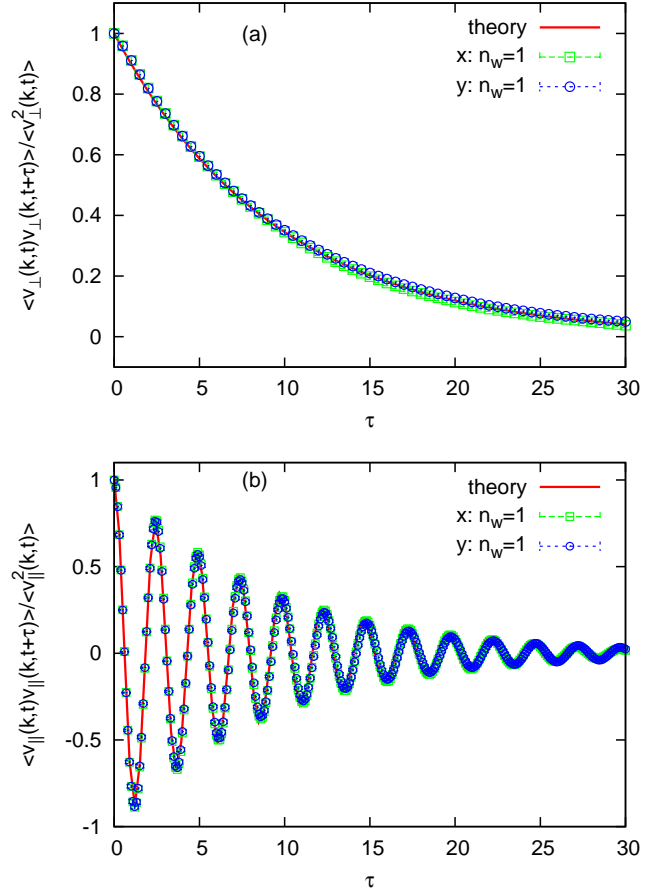

Figure 27: (Color online) Autocorrelation functions in Fourier space for DPD particles. (a) transversal component: shear viscosity $\eta = 1.077$ is taken from Ref. [51]. (b) longitudinal component: bulk viscosity and sound speed are measured to be $\zeta = 0.718$ and $c_T = 4.085$. Wave vectors are taken in both x and y directions for cross-validating while data in z are ignored. Error bars are smaller than the size of the symbol and cannot be seen clearly.

Appendix G: A note on no-slip boundary condition of SDPD

We briefly revisit an implementation of no-slip boundary condition in SDPD and point out a previously overlooked pitfall on fluctuation-dissipation balance near a solid wall [39].

Following early work on SPH method [37, 48, 56], an effective no-slip boundary between a fluid particle f and a solid boundary particle b can be achieved by maintaining a zero velocity at the fluid-solid interface. Assuming a linear interpolation of velocity between f and b, the zero velocity can be achieved, if b is dynamically assigned an artificial velocity as

$$v_b = \frac{d_b}{d_f}v_f, \quad \text{(G1)}$$

where v_f is the velocity of fluid particle f, d_f and d_b are distances of f and b to the interface, respectively. Therefore, the pairwise dissipative force between f and b is rescaled by α, compared to as if b was another fluid particle f',

$$\mathbf{F}_{fb}^D = \alpha \mathbf{F}_{ff'}^D, \qquad (G2)$$

$$\alpha = \frac{d_f + d_b}{d_f}. \qquad (G3)$$

A limitation in the previous work [39] is that the random force was not rescaled accordingly as

$$\mathbf{F}_{fb}^R = \alpha^{1/2} \mathbf{F}_{ff'}^R. \qquad (G4)$$

To show the effect of this limitation, we perform two SDPD simulations in box $[L_x, L_y, L_z] = [1, 1, 1]$ with two solid walls bounded at $y = 0$ and L_y. One simulation is without correction ($\alpha = 1$) on $\mathbf{F}_{fb}^R$ and the other is with correction using Eq. (G4). Results are compared in Fig. 28, where the importance of the correction using Eq. (G4) is apparent.

We note that this subtle correction was also previously taken care of in a similar implementation of DPD method [57].
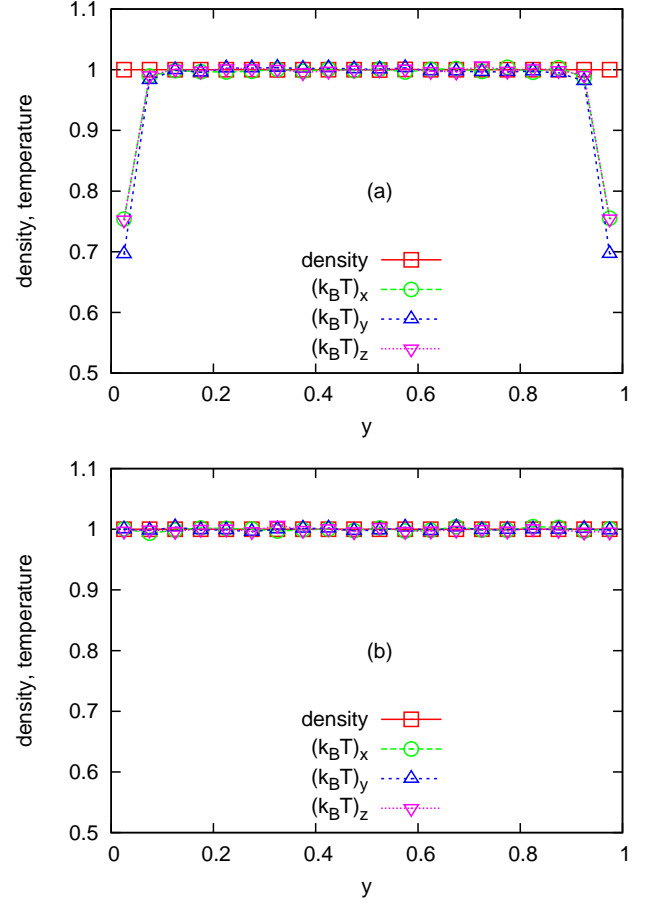

Figure 28: (Color online) Density and temperature profiles of wall-bounded SDPD. (a) without correction on random force: $\alpha = 1$. (b) with correction on random force: $\alpha = (d_f + d_b)/d_f$.

[1] L. D. Landau and E. M. Lifshitz, *Fluid mechanics*, Course of theoretical physics, Vol. 6 (Pergamon Press, Oxford, 1959).

[2] J. B. Bell, A. L. Garcia, and S. A. Williams, Phys. Rev. E **76**, 016708 (2007).

[3] J. Kordilla, W. Pan, and A. Tartakovsky, The Journal of Chemical Physics **141**, 224112 (2014).

[4] A. J. C. Ladd, Phy. Rev. Lett. **70**, 1139 (1993).

[5] P. J. Hoogerbrugge and J. M. V. A. Koelman, Europhys. Lett. **19**, 155 (1992).

[6] P. Español and P. Warren, Europhys. Lett. **30**, 191 (1995).

[7] R. D. Groot and P. B. Warren, J. Chem. Phys. **107**, 4423 (1997).

[8] G. Gompper, T. Ihle, D. Kroll, and R. Winkler, in *Advanced Computer Simulation Approaches for Soft Matter Sciences III*, Advances in Polymer Science, Vol. 221, edited by C. Holm and K. Kremer (Springer Berlin Heidelberg, 2009) pp. 1–87.

[9] P. Español and M. Revenga, Phys. Rev. E **67**, 026705 (2003).

[10] M. Grmela and H. C. Öttinger, Phys. Rev. E **56**, 6620 (1997).

[11] A. Vázquez-Quesada, M. Ellero, and P. Español, J. Chem. Phys. **130**, 034901 (2009).

[12] M. Serrano and P. Español, Phy. Rev. E **64**, 046115 (2001).

[13] G. De Fabritiis, M. Serrano, R. Delgado-Buscalioni, and P. V. Coveney, Phys. Rev. E **75**, 026307 (2007).

[14] S. Litvinov, M. Ellero, X. Y. Hu, and N. A. Adams, Phys. Rev. E **77**, 066703 (2008).

[15] A. Vázquez-Quesada, M. Ellero, and P. Español, Microfluid Nanofluidics **13**, 249 (2012).

[16] X. Bian, S. Litvinov, M. Ellero, and N. J. Wagner, J. Non-Newton Fluid Mech. **213**, 39 (2014).

[17] K. Müller, D. A. Fedosov, and G. Gompper, Scientific Reports **4**, 4871 (2014).

[18] H. Lei, C. J. Mundy, G. K. Schenter, and N. K. Voulgarakis, The Journal of Chemical Physics **142**, 194504 (2015).

[19] J. P. Hansen and I. R. McDonald, *Theory of simple liquids*, 4th ed. (Elsevier, 2013).

[20] J. P. Boon and S. Yip, *Molecular Hydrodynamics* (Dover Publications, Inc., New York, 1991).

[21] S. T. O'Connell and P. A. Thompson, Phys. Rev. E **52**, R5792 (1995).

[22] N. G. Hadjiconstantinou and A. T. Patera, International Journal of Modern Physics C **08**, 967 (1997).

[23] X. B. Nie, S. Y. Chen, W. N. E, and M. O. Robbins, J. Fluid Mech. **500**, 55 (2004).

[24] W. Ren and W. E, J. Comput. Phys. **204**, 1 (2005).

[25] T. Werder, J. H. Walther, and P. Koumoutsakos, J. Comput. Phys. **205**, 373 (2005).

[26] G. De Fabritiis, R. Delgado-Buscalioni, and P. V. Coveney, Phys. Rev. Lett. **97**, 134501 (2006).

[27] R. Delgado-Buscalioni and G. De Fabritiis, Phys. Rev. E **76**, 036709 (2007).

[28] M. Praprotnik, L. Delle Site, and K. Kremer, Annu. Rev. Phys. Chem. **59**, 545 (2008).

[29] R. Delgado-Buscalioni, K. Kremer, and M. Praprotnik, J. Chem. Phys. **128**, 114110 (2008).

[30] D. A. Fedosov and G. E. Karniadakis, J. Comput. Phys. **228**, 1157 (2009).

[31] P. Neumann, W. Eckhardt, and H.-J. Bungartz, Computers & Mathematics with Applications **67**, 272 (2014).

[32] N. D. Petsev, L. G. Leal, and M. S. Shell, The Journal of Chemical Physics **142**, 044101 (2015).

[33] X. Bian, Z. Li, and G. E. Karniadakis, Journal of Computational Physics **297**, 132 (2015).

[34] Y.-H. Tang, S. Kudo, X. Bian, Z. Li, and G. E. Karniadakis, Journal of Computational Physics (2015).

[35] J. J. Monaghan, Rep. Prog. Phys. **68**, 1703 (2005).

[36] J. Bonet and T.-S. L. Lok, Comput. Method. Appl. Mech. Eng. **180**, 97 (1999).

[37] J. P. Morris, P. J. Fox, and Y. Zhu, J. Comput. Phys. **136**, 214 (1997).

[38] J. J. Monaghan, J. Comput. Phys. **110**, 399 (1994).

[39] X. Bian, S. Litvinov, R. Qian, M. Ellero, and N. A. Adams, Phys. Fluids **24**, 012002 (2012).

[40] W. Dehnen and H. Aly, Mon. Not. R. Astron. Soc. **425**, 1068 (2012).

[41] D. J. Price, J. Comput. Phys. **231**, 759 (2012).

[42] For example, for the transversal autocorrelation function (ACF) in Eq. (21a), one can take $u(\mathbf{x}_i,t) = \delta v_y(\mathbf{x}_i,t)\rho(\mathbf{x},t)$ and $\mathbf{k} = (2\pi n_w/L_x, 0)$, or one can also take $u(\mathbf{x}_i,t) = \delta v_x(\mathbf{x}_i,t)\rho(\mathbf{x},t)$ and $\mathbf{k} = (0, 2\pi n_w/L_x)$, in total 2 combinatorial ways in $2D$ system for each $\mathbf{k}$. Similarly, there are also 2 combinatorial ways to calculate either the parallel ACF in Eq. (21b) or the density ACF in Eq. (21c). In $3D$ system, there are in total 6 combinatorial ways to calculate the transversal ACF and 3 combinatorial ways to calculate either the longitudinal ACF or the density ACF. Similarity can be drawn for the cross correlation functions (CCFs) in Eq. (21d)(21e). Combining results from all possible combinatorial ways may improve the statistics.

[43] J. Keiner, S. Kunis, and D. Potts, ACM Trans. Math. Softw. **36**, 19:1 (2009).

[44] G. Bohling, *Kriging*, Tech. Rep. (Kansas Geological Survey, University of Kansas, 2005).

[45] P. Goovaerts, *Geostatistics for Natural Resources Evaluation* (Oxford University Press, 1997).

[46] M. L. Stein, *Interpolation of spatial data some theory for Kriging* (Springer, 1999).

[47] G. Bohling, *Introduction to Geostatistics and Variogram Analysis*, Tech. Rep. (Kansas Geological Survey, University of Kansas, 2005).

[48] H. Takeda, S. M. Miyama, and M. Sekiya, Prog. Theor. Phys. **92**, 939 (1994).

[49] R. Delgado-Buscalioni and A. Dejoan, Phys. Rev. E **78**, 046708 (2008).

[50] J. T. Padding and A. A. Louis, Phy. Rev. E **74**, 031402 (2006).

[51] X. Fan, N. Phan-Thien, N. T. Yong, X. Wu, and D. Xu, Phys. Fluids **15**, 11 (2003).

[52] C. A. Marsh, G. Backx, and M. H. Ernst, Phys. Rev. E **56**, 1676 (1997).

[53] J. A. Backer, C. P. Lowe, H. C. J. Hoefsloot, and P. D. Iedema, J. Chem. Phys. **122**, 154503 (2005).

[54] C. Hijón, P. Español, E. Vanden-Eijnden, and R. Delgado-Buscalioni, Faraday Discuss. **144**, 301 (2010).

[55] Z. Li, X. Bian, B. Caswell, and G. E. Karniadakis, Soft

Matter **10**, 8659 (2014).

[56] X. Bian and M. Ellero, Comput. Phys. Commun. **185**, 53 (2014).

[57] H. Lei, D. A. Fedosov, and G. E. Karniadakis, J. Comput. Phys. **230**, 3765 (2011).